NATIONAL INSTITUTE FOR FUSION SCIENCE

Density Fluctuation in JIPP T-IIU Tokamak Plasmas
Measured by a Heavy Ion Beam Probe

Y. Hamada, A. Nishizawa, Y. Kawasumi, A. Fujisawa,
K. Narihara, K. Ida, A. Ejiri, S. Ohdachi, K. Kawahata, K. Toi, K. Sato,
T. Seki, H. Iguchi, K. Adachi, S. Hidekuma, S.Hirokura, K. Iwasaki, T. Ido,
M. Kojima, J. Koong, R. Kumazawa, H. Kuramoto, T. Minami, I. Nomura,
H. Sakakita, M. Sasao, K.N. Sato, T. Tsuzuki, J. Xu, I. Yamada and T. Watari

(Received - Oct. 29, 1996)

RESEARCH REPORT
NIFS Series

NAGOYA, JAPAN

Density fluctuation in JIPP T-IIU tokamak plasmas measured by a heavy ion beam probe

Y. Hamada, A. Nishizawa, Y. Kawasumi, A. Fujisawa, K. Narihara, K. Ida, A. Ejiri,

S. Ohdachi, K. Kawahata, K. Toi, K. Sato, T. Seki, H. Iguchi, K. Adachi,

S. Hidekuma, S. Hirokura, K. Iwasaki, T. Ido, M. Kojima, J. Koong, R. Kumazawa,

H. Kuramoto, T. Minami, I. Nomura, H. Sakakita, M. Sasao, K.N. Sato, T. Tsuzuki,

J. Xu, I. Yamada, and T. Watari

National Institute for Fusion Science, Nagoya, 464-01, Japan

Multiple and small sample-volume measurements of the density turbulence and potential profile measurement in tokamak plasmas were conducted by a heavy ion beam probe. The obtained wavenumber/frequency spectrum $S(k,\omega)$ shows that the cross-section of NBI heated plasmas is divided into three regions of different turbulence characteristics. Outside the reversal layer of poloidal propagation direction of density turbulence, a low-frequency and low-wavenumber mode with ion diamagnetic drift direction dominates. The region encircled by the reversal layer is divided into two parts at nearly perpendicular NBI heating, the region where the propagation velocity is near the E_r/B_t poloidal rotation velocity and the bad-curvature region of very small wavenumber and high propagation velocity. The region of high propagation velocity, found in NBI plasmas, disappears in ohmic plasmas. In addition, a small component which propagates in the ion diamagnetic drift direction is observed in NBI plasmas.

Keywords: tokamak, turbulence, HIBP, NBI

1. INTRODUCTION

Local measurement of plasma turbulence in a toroidal magnetic confinement device is very important, since the confinement property changes a lot across the minor radius. The H-mode is one of the most prominent example of local and drastic change of the confinement property. A heavy ion beam probe (HIBP) is one of the most competent methods for local measurement of the turbulence[1-6]. In addition, it may be a powerful diagnostic tool for the plasma turbulence because of the unique potentialities of the density, potential and magnetic measurement. However, the fundamental problem in the obtained results of the density turbulence at TEXT tokamak with an HIBP is that the dominant wavenumber (k) is much smaller than the value where the growth rate of the drift-wave instability is maximum[3-5]. The propagation velocity of the density turbulence is also much faster than the poloidal rotation velocity and diamagnetic drift velocity of the tokamak plasma. These results are in contradiction with the prediction of drift wave theory [4] and also with the experimental observations by microwave scattering[7,8,9] and beam emission spectroscopy (BES)[10,11].

In order to measure the k spectrum accurately we prepared a set of detection system for 7 sample-volume-measurement and tried to sharpen the injected beam to make the length of the sample volume as small as possible. In the turbulence study by an HIBP the size of the sample volume is a crucial physical quantity, since the obtained signal is the sum (average) of the ionization at the sample volume and the turbulence with large wavenumber is smoothed out. With multiple sample volume measurement, we are able to obtain the contour of the wavenumber/frequency spectrum density $S(k,\omega)$ just like by probe array measurement. By the small sample volume we are able to measure the wavenumber up to about 3 cm^{-1}. The detail of the method and its results will be described in the following sections.

2. EXPERIMENTAL APPARATUS AND METHODS

2.1. Tokamak system.

The JIPP T-IIU tokamak[12] is operated at 3 tesla. Its major radius is 93 cm with the minor radius of 23 cm. Nearly perpendicular neutral beam injection (NBI) of which injection line is tilted in the co-direction (the direction of the plasma current) by only 9 degrees, is employed. The main diagnostics are, a YAG Thomson scattering apparatus with 28 spatial measurement points and 100 H_z repetition rate for detailed profiles of plasma density and electron temperature, 8-channels- ECE polychromator, 6-channels- FIR interferometer and a charge recombination spectroscopy using NBI for ion temperature profiles. The YAG laser beam is injected from the upper port of the vacuum vessel to the lower port.

2.2. A heavy ion beam probe system.

A setup of the 500 keV HIBP[12 - 14] on the JIPP T-IIU tokamak is shown in Fig. 1(a). An accelerator is placed horizontally since it must be taken apart frequently in order to change a short-life ion source. A thallium beam is used. The beam (Tl^+) is bent into the tokamak by an electrostatic cylindrical deflector instead of a magnetic deflector because of the large mass number of the injected ions. The beam can be focused to a diameter of about 2 millimeter in the tokamak by a set of a cylindrical deflector and two electrostatic quadrupole lenses (doublet). The secondary beam (Tl^{++}) ionized at the sample volume enters the entrance slits of the energy analyzer. The injection current is a few tens of μA and the secondary beam current detected is about order of 0.1 μA. To reduce the photo-current at the detector due to the intensive radiation in the additionally heated plasmas, the two-staged optical trap shown in Fig, 1(a) is crucial.

The basic principle of local potential measurement by an HIBP is illustrated in Fig. 1(b). The energy change of the secondary beam from the injected energy of the primary beam corresponds to the local potential where the ionization occurs, since the total

energy of the secondary beam energy (E_{bt}) increases by the local potential of the ionization point due to the increase of the charge number[1]. This change of the beam energy is measured by a parallel-plate energy analyzer with an entrance angle of 30 degrees, which has the focus up to second order for the change of the in-plane entrance angle (the angle in the analyzer plane (the plane of Fig. 1(a))[16]. This parallel plate analyzer is intrinsically suitable for multiple sets of the entrance slit and a detector (many sample volumes) since the electric field is uniform. We put 7 sets of an input slit and detectors in order to get more information on the propagation of the turbulence[6], although the signals from 6 input slits are usually available with ordinary adjustment, because of the collisions of the secondary beam with the wall in the analyzer.

The primary and secondary beam are deflected into the toroidal direction by the poloidal magnetic field. The secondary beam enters the opening of an input-slit of the energy analyzer at horizontally displaced point and with finite out-of-plane entrance angle (ϕ_{op}) (perpendicular to the plane of Fig. 1(a)), which change due to the scan of the ionization point (sample volume). First of all, the analyzer must have a wide horizontal opening for the input slit and wide upper and lower plates for uniform characteristics to the displaced entrance of the secondary beam. Our analyzer has a shaped high-voltage upper plate to enlarge the region of the uniform electric field between the plates[17]. The change in the out-of-plane entrance angle causes large error in the measurement of the total beam energy and local potential in a high-voltage HIBP, because a parallel plate analyzer measures the beam energy of the motion in the analyzer plane (in-plane motion), (E_b) instead of the total kinetic beam energy , where the relation $E_b = E_{bt} \cos^2(\phi_{op})$ holds. In order to reduce the error we apply fast toroidal sweep at the entrance to the tokamak and measure radial potential profiles utilizing the dependence of $\cos^2(\phi_{op})$. The detail will be described later with experimental data.

The detector set of the secondary current is composed of stainless-steel upper and lower plates or left and right plates connected with low noise amplifiers. The change of the beam energy is measured by the change of the difference of the signals of upper and lower detector plates normalized by the intensity of the secondary current (sum of the

upper and lower detector currents) [18]. The local density fluctuation is considered to be proportional to the fluctuations of the sum, although the coupling of the density turbulence outside the sample volume must be taken into consideration. For the measurement of plasma turbulence, the stability of various power supplies in an accelerator, beam transport and energy analysis are very important. The stability of the voltages of the accelerator and the analyzer are nowadays greatly enhanced. The ripple of the electrostatic accelerating voltage of JIPP T-IIU HIBP is about 2 Vp-p out of 500 kV. We also reduced the high-frequency ripple of the voltage of an upper electrode of the energy analyzer to about 0.02 V out of 100 kV by use of LC filter in the SF_6 gas. The sampling rate at 12 bits AD conversion is 2 MHz and the frequency band width of the detector amplifier shows the 3 dB decrease of gain at 300 kHz. The intensity of the injected ion beam is typically about 30 μA.

2.3. Shape of sample volumes.

Figure 2 shows the calculated position and shape of the sample volume for the measurement discussed in this paper, when the primary beam (450, 350, 300, 250 and 200 keV) is swept in stepwise, in the poloidal direction by the sweeper which is located before the entrance to the tokamak as is shown in Fig. 1. The calculation of the shape and position is performed assuming that a parallel thallium beam with the diameter of 1.5 mm at the poloidal entrance sweeper, is injected into the 3 tesla toroidal field. The shape of sample volumes is like a rhombus as is shown in Fig. 2(b). The parameters of the sample volume are summarized in Table 1.

The smallness of the sample volume is essential for the turbulence measurement by HIBP, since it determines the detectable maximum wavenumber, together with the distance between them through Nyquist wavenumber. In the case of large sample volume, the turbulence with short wavelength is difficult to detect accurately since these fluctuations are smoothed out at the detector. We roughly simulate the detector collection function with Gaussian $e^{\frac{-4x^2}{l_s^2}}$, where l_s is the longer diagonal length of the rhombus-like

sample volume and the x is the distance form the gravity center of the sample volume in the longer direction. The efficiency of the detection of the turbulence with wavenumber k in this direction, is estimated as $e^{-(l_s k)^2}$ and the maximum k number may be equal to $1/l_s$, since the relation $\int_{-\infty}^{\infty} e^{ikx} e^{-\alpha x^2} dx \propto e^{-\frac{k^2}{4\alpha}}$ holds.

The width of the rhombus of the sample volume in Fig. 3(b) corresponds to the opening of the entrance slit (in this experiment, 3 mm). On the other hand, the length is proportional to the diameter of the beam and becomes large if the angle of the beam trajectory to the observation line is small. The assumption of the parallel beam may be justified because the beam is focused to the plasma center after the long free travel from the cylindrical deflector to the tokamak as shown in Fig. 1(a). The position and size of the sample volume are strongly dependent on the injection angle, position of the beam at the entrance sweeper , and the beam size. We controlled the beam position, injection angle and beam size to constant values by the beam profile measurement by two beam profile monitors 3, 4 on the straight section of the trajectory of the primary beam as shown in Fig. 1(a). Also, inside the tokamak vessel we installed beam size monitor (several wires) and measured the beam size by sweeping the beam.

The calculated beam size is small by about factor 2 or 3, compared to the previous 500 keV HIBP experiments [3]. There is also no overlapping of adjacent sample volume along the trajectory of primary beam as is shown in Fig. 2(b). This smallness and no overlapping may be partially verified in Fig. 3. Figure 3 shows the intensity of the secondary beam current (s_j) (sum of the upper and lower plate currents) of 6 sample volumes (j =1 to 6) as the position of the sample volume is swept in 7 steps (1 to 7) as shown in Fig. 2 for 450 keV case. The start of the sweep is at 200 ms under NBI heating. The sample volumes are swept from plasma boundary to the inner region of the plasma by changing the poloidal sweep voltage. The sweep angle at step m, (θ_m) in degrees is $\theta_m = 0.4 \times m - 0.9$. The total injection angle of the injected beam is 53.0 + θ_m. The intensity of the secondary beam in Fig. 3 decreases due to the beam attenuation as the sample volume approaches the plasma center. Near the plasma center it suddenly

decreases to almost zero because the secondary beam is scraped off by the lower part of the horizontal port as is shown in Fig. 1(a). From the decaying feature of the intensities of 6 sample volumes (SV 1 to SV 6) due to the collision, we are able to estimate approximately the size of the sample volumes which determines the upper limit of the wavenumber measurement. As shown in Fig. 3, the intensity of SV 1, s_1 decays almost completely at the transition from step 5 to step 6, while s_2 regularly decays and shows almost no sign of collision with a wall. At the transition from step 6 to step 7, s_4 decays greatly while s_5 decays regularly. These facts mean that the length of the sample volume is shorter than the distance between the gravity centers of the nearby sample volumes. This result agrees with the calculations of the shape of the sample volume based on the measured diameter of the beam shown in Fig. 2(b). The behaviour of s_6 is different from the signals from other sample volumes. It is due to the collision of the secondary beam to the wall at the analyzer because of the large change of the entrance angle to the analyzer. The gain of the detector is also different for SV 5 and SV 6.

2.4. Method of turbulence measurement.

For the local measurement of the turbulence, many time-segments of data at spatially fixed point are required, while scanning of the sample volume from the plasma surface to inner region in a shot is advantageous. Accordingly, we scanned the sample volume across the plasma in stepwise, while fixing them for 5 ms at one step as shown in Fig. 3.

At each step, the s_j is analyzed by correlation method and two-dimensional (spatial and time) Fourier analysis for $S(k,\omega)$. The correlation coefficient function $\rho_{i,j}(t)$ of the signal $s_i(t)$ at i-th sample volume and $s_j(t)$ at k-th sample volume is described by the following formula,

$$\rho_{i,j}(\tau) = \frac{C_{i,j}(\tau)}{\sqrt{C_{i,i}(0)}\sqrt{C_{j,j}(0)}}, \tag{1}$$

where $C_{i,j}$ (t) is cross correlation function defined as $C_{i,j}(\tau) = \int_{-\infty}^{\infty} \tilde{s}_i(t)\tilde{s}_j(t+\tau)dt$. The

integration time in the correlation coefficient functions is 2.0 ms in this paper instead of -

infinity to infinity. Correlation curves obtained in this paper are statistically reliable

because of the high signal to noise ratio. The similar correlation curves are obtained even

if we reduce the integration time to 0.4 ms.

$S(k,\omega)$ is calculated through the following equation, $S(k,\omega) = \langle |s(k,\omega)|^2 \rangle$, where

$s(k,\omega)$ is the two-dimensional Fourier transform of the set of $\dfrac{\tilde{s}_j}{s_j}$ for 100 µs duration.

Here, the $< >$ is the averaging for 40 realizations (4 ms). The range of the wavenumber

measurement by the finite number (n, in this case n=6) of the sample volume is from

k_{max} , to $- k_{max}$ where $k_{max} = \pi/d_{sv}$ (Nyquist wavenumber) and d_{sv} is the distance

of each sample volume separation. This range of wavenumber is covered by n

independent wavenumber measurements ranging from, $(1 - n/2)k_0$ to $(n/2)k_0$ in case of

even n, where $k_0 = 2\pi/(nd_{sv})$. In our analysis the separation of the each sample volume

is assumed to be the same for simplicity.

We changed the beam energy and performed the turbulence measurement in order to

cover the wide area of the plasma cross-section.

3. EXPERIMENTAL RESULTS

3.1. Density, temperature and potential profiles.

The experiment is usually performed at the average density of less than $5 \times 10^{13}/cm^{-3}$

to avoid strong beam attenuation due to high density plasmas. In this paper, NBI and OH

heated plasmas with a plasma current of about 170 kA ($q_a = 6$) were studied. The nearly

perpendicular NBI is injected from 175 ms to 300 ms. The plasma current started at 50

ms and reached its peak at about 70 ms.

Figure 4 shows changes of radial profiles of the electron temperature and density, measured by the YAG laser Thomson scattering apparatus[18]. The first (lowest) profile in Fig. 4 is at 160 ms in OH phase. Ten profiles at every 20 ms are presented and shifted upwards to avoid the confusion. At 175 ms (between the first and second profile) the injection of about 0.5 MW NBI heating started and lasted for 125 ms. The increase of the plasma density due to the NBI heating is observed and lasted throughout the NBI pulse length as is shown in Fig. 4. The electron temperature is not affected by NBI and stays nearly constant. Also radial profiles of the electron diamagnetic drift velocity,

$$V_{d,e} = \frac{n_e(r_j)}{\dfrac{d(n_e(r))}{dr}} \frac{T_e}{m_e \omega_{ce}}$$ are calculated using these experimental data and are shown in Fig.

4(c). The electron diamagnetic velocity is zero near the center of the plasma and reaches the peak of about a little less than 2 km/s at about $r = a_p/4$ and gradually decreases to zero.

Figure 5 shows how the radial potential profile evolves throughout OH and NBI-heated JIPP T-IIU plasma discharges, utilizing the HIBP. As mentioned above, the measurement of the radial potential profile in one radial sweep is usually rather difficult for a high voltage HIBP, since the out-of-plane entrance angle (ϕ_{op}) as well as in-plane entrance angle change considerably during the radial scan of sample volumes. The error induced by the change of out-of-plane entrance angle in one radial scan is larger than usual plasma potential well of a few kV in the case of 500 keV HIBP. We compensate this error by the application of the fast toroidal sweep and slow radial poloidal sweep at the entrance to the tokamak[13]. At the third radial potential profile of Fig. 5 for example, the radial scan is performed from 91 ms and ends at 93.5 ms. During this period, about 12 fast toroidal sweeps are applied. By the toroidal sweep, the secondary beam in the analyzer can be parallel to the symmetry plane of the analyzer ($\phi_{op}=0$) at one time. At this time the potential beam energy can be local maximum as is shown clearly in Fig. 5 and the potential reduced from the change of the beam energy, is free from the error because of the dependence of $E_b = E_{bt}\cos^2(\phi_{op})$. By connecting many peaks (local maxima) due to the toroidal deflections in Fig. 5, we can get a radial potential profile (a dashed curve). The static space potential of the tokamak plasma is expected to have toroidal symmetry and the

deviation of the sample volume from the original magnetic surface is very small when toroidal sweep angle is small. We scanned radially by 400 Hz and applied a 5 kHz fast toroidal sweep.

The first radial profile in Fig. 5 which starts at 51 ms (ts = 51 ms) is 3 ms after the application of the toroidal electric field to drive the plasma current. It is taken at the very early phase in the plasma start up (less than a few kA of the plasma current). The depth of the potential well is very shallow since it is in the breakdown phase. The profile is almost the same with the calibration curve of the analyzer for the change of the in-plane entrance angle (plane of Fig. 1(a)) of the secondary beam. This change is caused by the poloidal scan of the sample volume[13]. The depth of core potential rapidly grows and reaches nearly full depth in 20 ms as shown in the next profile of Fig. 5. The NBI in this case starts at 100 ms, and the potential depth does not change significantly because it is almost perpendicular injection. The average electric field at about $a_p/4$ for ts=170 ms during NBI phase, (deduced from subtraction of dashed curves of the first curves to the curve in the seventh figure) is about 10 kV/m. This electric field is rather uniform across the cross-section as was observed in the TEXT tokamak [20] and does not change appreciably in time. The poloidal electric drift velocity given by E_r / B_t is about 3 km/s.

The ion temperature profile in the JIPP T-IIU tokamak is obtained by the charge exchange recombination spectroscopy (CXRS) utilizing the injected NBI beam [20]. Figure 6 shows the ion temperature profiles in the similar discharges. The ion temperature attains the peak value in less than 20 ms and saturates throughout the NBI pulse.

3.2. Turbulence in NBI heated plasma.

First of all, we can state that the measurement of the density turbulence has a high signal to noise ratio, by the comparison of raw data of Fig. 3 when the sample volume is inside (step 1 to 7) and outside the plasma (step 0, indication of noise level). The main noise in the turbulence measurement is due to the amplifier noise in the detector circuits

instead of the photo-electrons caused by the radiation from the plasma. In addition, a close look of the intensity of Fig. 3 showed us that $\frac{\tilde{s_j}}{s_j}$ which may be proportional to $\frac{\tilde{n_e}}{n_e}$ at the sample volume, where $\tilde{s_i}(t) = s_i(t) - \overline{s_i(t)}$, is larger near the plasma boundary and it decreases as the sample volume is swept into the plasma center as is shown in Fig. 3. Also we can see that the density turbulence at the plasma boundary is dominated by the low frequency fluctuations.

Figure 7 shows behaviours of 6 correlation coefficient functions $\rho_{1,j}(t), j), j=1,2,3,4,$ 5, 6 of the secondary current intensities of 6 sample volumes $(s_j, j=1$ to 6) shown in Fig. 3 and contours of wavenumber/frequency spectrum density $S(k,\omega)$ at 6 steps for 450, 350, 300, 250, 200 keV primary beam energy.

The right ordinate of the contour of $S(k,\omega)$ is the wavenumber (k_1) along the array of the sample volumes, while the left ordinate (k_p) is along the circular magnetic surface. Assuming zero phase shift of the turbulence in the radial direction as is observed in BES and FIR scattering experiment[9,10], we may be able to relate these quantities in the following way, $k_p = k_1 / |n_r \times n_s|$, n_r and n_s are unit vectors along the minor radius and along the array of sample volumes, respectively. The experimetal evidence of zero phase shift in HIBP measurement when the direction of the sample volume array is normal to magnetic surface, will be discussed later to support this assumption.

A. Turbulence near plasma boundary.

One of the most outstanding change in the correlation coefficient functions and $S(k,\omega)$ of various position of sample volumes in Fig. 7, may be at the plasma boundary typically for 200 keV case. Near the plasma boundary, the correlation time in correlation coefficient functions becomes very long as shown in all steps of Fig. 7(e) [24]. The sharp transition from short to lone correlation time occurs between step 1 and step 2 and between step 3 to step 4 of Fig. 7(d). This transition is accompanied by a reversal on the poloidal propagation direction of the turbulence from the electron diamagnetic drift direction to ion diamagnetic drift direction [22, 3, 23,24]. The propagation of the

turbulence can be more easily determined by the correlation curves instead of $S(k,\omega)$. Outside the reversal layer the turbulence is characterized by the long correlation time and the propagation into ion diamagnetic drift direction. We may call this mode as ' edge ion mode', following the study of tokamak turbulence by BES[10,11]. We also call the mode which propagates in the electron diamagnetic drift direction as 'electron mode'. The position of this reversal layer depends on the discharge conditions. At NBI heating phase, it moves outwards.

We can also observe in $S(k,\omega)$ of Fig. 7(e) that the low-frequency turbulence dominates in this region and the average wavenumber is much smaller than the 1.0 cm $^{-1}$. This small wavenumber outside the reversal layer measured by our HIBP (non-perturbing and very local method) is similar to the result by BES at the TFTR edge plasma [11] and may be smaller than one measured by a Langmuir probe and FIR scattering [22-24].

B. Turbulence in the "normal" region.

By a shift of peaks of cross correlation coefficient functions and also by connecting the hills in a contour of $S(k,\omega)$ in the inner region, we are able to state that the main turbulence propagates in the electron-diamagnetic-drift direction in the upper region (steps 2, 3,4,5 for 450 keV and steps 2 and 3 for 350, 300, 250 keV) as shown in Fig. 7. As for the shift of peaks of correlation curves at step 4 (450 keV) for example, the shift time ($\Delta\tau_{sh}$) between SV 6 to SV 1 is $\Delta\tau_{sh} = 7$ μs and the distance between the center of the SV 6 to 1 d_{sv} is about 4 cm. The propagation time determined by the correlation curves (5.0 x d_{sv} / $\Delta\tau_{sh}$) is about 6 km/s, while the dashed straight line in $S(k,\omega)$ of the step 3 (450 keV) is on the point of 100 kHz and $k_l=1$ cm^{-1} and $k_p = 2$ cm^{-1}(wavenumbers along the sample volume array (l) and along the poloidal magnetic surface (p)). The phase velocity (ω/k_l) along the array is 6 km/s. As shown in this example, the phase velocity obtained by the curve connecting the hill in a contour plot using the wavenumber along the sample volume array, generally agrees with the propagation velocity determined by the shift of the peak of the correlation curves.

In this case, the phase velocity of the turbulence along the magnetic surface (ω/k_p) is 3 km/s, under the assumption of no phase shift in radial direction. The radial electric field shown in Fig. 4 is about 10 kV/m, leading to the poloidal drift velocity E_r/B_t of about 3.3 km/s. Since the electron diamagnetic drift velocity at the step 4 (450 keV) is about 1.5 km/s since $r/a_p = 0.3$. Accordingly, we may state that the laboratory-frame propagation velocity of the turbulence is very similar to the fluid velocity of the electric drift velocity, which is a little faster than the electron diamagnetic drift velocity. In this sense we call the turbulence "normal". The poloidal propagation characteristics in the laboratory frame may be greatly modified by the toroidal rotation velocity, since these turbulence may have the phase dependence of $e^{i(k_\theta\theta + k_\phi\phi)}$[10,11]. In our nearly perpendicular NBI plasma, the maximum toroidal rotation velocity (V_t) measured by CXRS is about 15 km/s and the direction is opposite to the plasma current (counter direction) as in OH and ICRF heated plasmas, although the injection is tilted to co-injection by 9 degrees[25]. Since the toroidal rotation may be equivalent with a poloidal rotation velocity of V_t $(R/r)/q$ with respect to the turbulence propagation in the laboratory frame, its effect is smaller than the poloidal electric drift velocity (E_r/B_t). The discussion on the propagation velocities of the turbulence in the plasma frame is, however, difficult due to the difficulties of the precise potential profile measurement by a high voltage HIBP and lack of the data for the profile of toroidal rotation velocity in this series of the experiment.

C. Propagation "anomaly"

Turbulence in the outer region (region of larger major radius and bad-curvature, step 6 for 450 keV, steps 4, 5, 6 for 350 keV, steps 3, 4, 5 for 300 keV of Fig. 7) tends to have very small wavenumber and do not show the characteristics into one direction in spite of the poloidal rotation in NBI heated plasmas. This region is shown as the shaded area in Fig. 3. For 200 and 250 keV cases, this character is not as prominent as 300 and 350 keV. For 200 keV case, the correlation curves show the edge ion mode characteristics (longer correlation time and dominance of the low frequency mode) for 200

keV case, since the sample volumes are fairly outside. For 250 keV case, the wavenumber is not so small and the propagation into the electron diamagnetic drift direction is clearly observed in steps of 2 and 3. The other steps become to the edge ion mode.

The wavenumber in this shaded area is very small and the phase velocity is much faster than the electric drift and diamagnetic drift velocities. In addition, the correlation coefficient function is not a monotonic function of the distance as is shown in step 3 of 300 keV case. In this sense we call the turbulence in this region as "anomalous" since it is different from the ordinary drift-wave theory[4]. These observations are constantly observed only in NBI plasmas as we discuss later.

3.3. Turbulence in OH plasmas.

The anomalous propagation characteristics of the turbulence observed in the bad-curvature region (shaded region in Fig. 3(a)) occur only in the NBI heated plasmas. Figure 8 shows the contours of $S(k,\omega)$ of OH plasmas at 350 and 300 keV cases, where the anomaly is very prominent in NBI plasma. In this case the turbulence at the shaded region of Fig. 2(a) propagates into the electron diamagnetic drift direction with the velocity comparable to the electric rotation velocity. The "anomalous" region changes into the "normal" region.

By looking at the correlation functions and contours of step 6 in 300 keV case (Fig. 8(b)), we can observe very small shift time of the peaks of the correlation coefficient functions and the dominance of the component of very small wavenumber in the contour of $S(k,\omega)$. The direction of the sample volume array in this case is almost along minor radius of the plasma as is shown in Fig. 2(a). As is shown in this example, we observe constantly that the propagation velocity of the turbulence is very sensitive to the angle between the direction of the array of the sample volumes and the direction along the minor radius. Accordingly, the assumption of zero phase shift of the turbulence normal

to the magnetic surface in the calculation of the wavenumber along the magnetic surface, may be justified.

3.4. Turbulence propagating in the ion diamagnetic drift direction.

The contours of $S(k,\omega)$ in step 2 of Fig. 7(a) show the existence of two modes of the turbulence propagating into different directions although the component propagating into the ion diamagnetic drift direction is small. It has a clear dip at $k = 0$, compared to the other contours of $S(k,\omega)$, and the fluctuation propagating in the ion diamagnetic drift directions is clearly observed. This mode is not observable at ohmic plasmas. It also differs from the mode propagating in the ion diamagnetic drift direction near the plasma boundary, because this mode has a finite wavenumber of about -1 cm^{-1} and the frequency of this mode extends up to a few 100 kHz.

Figure 9 shows the correlations and contours with fines steps around step 2 and 3 in Fig. 7(a). The injection angle at step m of Fig. 8 is $\theta_m = 0.16m - 0.4$, compared to $\theta_m = 0.4m - 0.9$ in case of Fig. 7(a). The frequency range is taken from -300 kHz to 300 kHz to show clearly the Doppler effect of the poloidal rotation velocity on the propagation characteristics. The $S(k,\omega)$ with $+ -$ frequency range clearly shows the existence of the turbulence propagating into the ion diamagnetic drift directions. The ion diamagnetic drift velocity which can be determined in Fig. 6 is similar in magnitude to the electron diamagnetic drift velocity and is small compared to the poloidal electric drift velocity. This mode may be similar to the core ion mode in TFTR [10] or similar to the ion mode observed in TEXT high-density OH plasmas by FIR scattering experiment [9] in terms of the propagation direction and the frequency. The HIBP measurement in the high density plasmas is impossible in our case because of the strong attenuation of the primary beam. The ratio of its amplitude of the turbulence propagating in the electron diamagnetic drift direction is about one fourth as is observed in TEXT.

4. DISCUSSIONS

4.1. Comparison with results from other tokamaks.

So far, the local measurement of density turbulence in a core tokamak plasma has been performed by HIBP and BES [2-6, 10,11]. The propagation velocity of the turbulence in the "normal" region measured in this experiment is considerably smaller than the velocity obtained at the old 500 keV HIBP experiment in the TEXT tokamak [3,4,5]. The TEXT HIBP measurement showed the phase velocity is about 20 km/s, about a factor 4 or 5 faster than the electric drift velocity near the center of the plasma and decreases towards the reversal layer [3, 5]. The region outside the reversal is not measured in detail. In addition, in TEXT the dominant wavenumber is found in the region of about $k\rho_i = 0.03$ or so, while in our measurement, $k\rho_i \approx 0.15$, where ρ_i is the ion Larmor radius. The reason for these differences may be due to the smaller sample volumes in our case, leading to the measurement of higher wavenumber and smaller phase velocity.

The intensive study of the density turbulence of NBI heated supershot plasmas in TFTR by BES were reported by Fonck et al [10,11]. They reported the presence of the 3 regions of different characteristics of turbulence. At boundary plasma the edge ion mode is observed. There is a transition layer between core ion mode and the edge ion mode, in which the fast electron mode which has the peak at 1 cm^{-1} in wavenumber and has high phase velocity and the edge ion mode are observed. In the core region the turbulence propagates in the ion diamagnetic drift direction in the plasma frame. Our observation of the edge ion mode by 200 keV beam is very similar to the BES results at TFTR in terms of low wavenumber smaller than 1 cm^{-1} and long coherence time. The long coherence time as long as 50 μs was also observed in ASDEX edge plasma, but the reported dominant wavenumber is about 1 cm^{-1} [25]. This value may be higher that those from our HIBP and BES measurements.

The transition layer in the very high temperature plasma in TFTR may be similar to our core plasma with NBI heating in terms of the ion and electron temperature and density. This prediction is not true. In our case, in the core region of OH plasma, only

the turbulence which propagates slowly in the electron diamagnetic drift direction is observed. In NBI heated plasma, the turbulence with very small wavenumber is localized only in the bad curvature region.

The β_t and β_p are about 0.01 and 1.0 in our NBI heated plasmas studied by HIBP, since the high density plasma is difficult to study by strong attenuation of the primary beam. The turbulence of "anomalous propagation" in our case may be by the nearly perpendicular NBI heating in JIPP T-IIU.

4.2.   Path integral effect.

The observation of the turbulence with very small wavenumber in our NBI heated plasma may be caused by non-local effect in the HIBP turbulence measurement (path integral effect) [26].   The intensity of the secondary beam is described by the following equation,

$$s_j = \sigma_{1,2} n_e(r_j) dl_j \; I_{bo} \exp\{-\int_{a_p}^{r_j} \sigma_{1,2} n_e(l) dl\} \exp\{-\int_{r_j}^{a_p} \sigma_{2,3} n_e(l) dl\}, \qquad (2)$$

where r_j is the position of the sample volume j, and the integrals are along the primary and secondary trajectories. dl_j is the length of the sample volume. Fluctuations of the plasma density at all the places on the primary and secondary beam trajectories, can influence s_j through attenuation of the primary and secondary beam (path integral effect) as shown in equation 2.   This effect is very universal and occurs in all beam probing measurements. Linearizing this equation, we can get

$$\frac{\tilde{s}_j}{\bar{s}_j} = \frac{\widetilde{n_e(r_j)}}{\overline{n_e(r_j)}} - \overline{n_e(r_j)} \left\{ \int_{a_p}^{r_j} \sigma_{1,2} \frac{\widetilde{n_e(l)}}{\overline{n_e(r_j)}} dl + \int_{a_p}^{r_j} \sigma_{2,3} \frac{\widetilde{n_e(l)}}{\overline{n_e(r_j)}} dl \right\}. \qquad (3)$$

Since the ratio of the ionization cross-section of the primary beam to that of the secondary beam $\sigma_{1,2} / \sigma_{2,3}$ is about 3 to 4, the effect on the coupling due to the attenuation of the primary beam may be larger. The effect of the path integral on the primary beam trajectory from the plasma boundary to the sample volume 6 should appears at the $k=0$ in the $S(k,\omega)$, since this effect contributes equally and without time delay to s_j, $j=1$ to 6 as is observed in equation (3). The $S(k,\omega)$ in the normal region (in the steps to 2 to 5 in Fig. 7(a) for example) shows only very small irregularities in the contours at $k=0$ and we may assume this effect is small. We are able to give a clear experimental evidence by multiple-sample-volume measurement to the statement that the high-voltage HIBP are free from the path integral effect if the density is not too high[26]. In the anomaly region, however, the main component is near $k=0$ and we have to evaluate the effect of the path integral effect carefully.

To determine whether the path integral effect is dominant or not, we provided new data set of 5 signals, $\dfrac{\tilde{s_j}}{\bar{s_j}} - \dfrac{\tilde{s_6}}{\bar{s_6}}$, $j=1$ to 5 instead of 6 signals s_i, $i=1$ to 6, and Fourier analyzed two-dimensionally. By this data set, we can suppress the contribution of the path integral from the plasma boundary to the sample volume 6 (integral on long distance). The path integral effect due to the integral between each sample volume, $\dfrac{\widetilde{n_e(l)}}{n_e(r_j)}\{\overline{n_e(r_j)}\ \sigma_{1,2} dl\ \}$,

where dl is the distance between the sample volumes, is small, compared to $\dfrac{\widetilde{n_e(l)}}{n_e(r_j)}$, since

$\{\overline{n_e(r_j)}\ \sigma_{1,2} dl\ \} < 0.1$ in these cases. This is also observed in the Fig. 3. The mean values of the sum signals on the same steps are nearly the same except the difference on the sensitivity of the detector plates as shown in Fig. 3. Rather large difference in the mean values of the different steps is due to the fact that the difference in the sweep angle causes different trajectory to the sample volume. This causes larger difference in the distance of the trajectory from the plasma boundary to the sample volumes compared to the distance between the sample volumes in different steps. The attenuation between the sample volumes in the same step even near the plasma core is not large. Accordingly, the contribution of the turbulence on the whole trajectory of the primary beam may be important as was suggested in the theoretical analysis[26], which scales as

$\dfrac{\widetilde{n_e(l)}}{n_e(r_j)} \{\overline{n_e(r_j)}\ \sigma_{1,2}\ l_c\}$ and $\sqrt{\left\langle \left|\dfrac{\widetilde{n_e}}{n_e}\right|^2\right\rangle} L_1 l_c (\sigma_{1,2}\overline{n_e})^2$ where L_1 is the arc length of the

primary trajectory and l_c is the correlation length. The first term is small as l_c is

comparable to dl. The second term can be a little larger than the first term because L_1 is

much larger than l_c . These contributions can be omitted in this data set.

Figure 10 (b) shows the contours of $S(k,\omega)$ based on $\dfrac{\widetilde{s_j}}{s_j} - \dfrac{\widetilde{s_6}}{s_6}$, $j =1$ to 5, in case of

Fig. 7(b), while Fig. 10(a) is based on $\dfrac{\widetilde{s_j}}{s_j}$ for direct comparison. Both figures show

basically the same characteristics, the dominant mode of very small wavenumber.

Accordingly, we may be able to state that in the "anomalous region" the path integral effect

is not significant.

The path integral effect is more severe in high density case, since the coupling is

through the attenuation. The intensity of the secondary beam is larger and attenuation of

the beam is smaller (lower local density) in case of step 4 in Fig. 7(b) than that of step 5 of

Fig. 8 (350 keV, OH plasma). Since in OH plasma, propagation is not "anomalous",

which means that path integral effect is not dominant, the case of step 4 in Fig. 7(b)

should be free from domination of path integral effect.

These differences of the $S(k,\omega)$ in 300, 350 and 450 keV cases in the anomaly region

shows clearly the toroidal (ballooning) nature of the turbulence in the outer region of the

NBI tokamak plasmas. Although our measurement in HIBP is inaccessible to the region

of smaller major radius, because of the collision of the secondary beam with the horizontal

port, there is a large difference in the $S(k,\omega)$ when the sample volumes are at the bad

curvature and at the neutral curvature (the direction of the density gradient makes an angle

of 90 degrees to the direction of the curvature).

CONCLUSION

Our results will be summarized as follows. Multiple and small sample-volume

measurements of the density turbulence and potential profile measurement in JIPP T-IIU

tokamak HIBP showed that in the OH plasma the phase velocity of the turbulence is near the poloidal electric drift velocity (E_r/B_t) except the plasma edge, in contrast to the previous 500 kV TEXT HIBP results.

It also showed that the tokamak cross-section under nearly perpendicular NBI heating, is divided into three regions, the low-k edge ion region outside the reversal layer, the bad- curvature low-k region and the "normal region" where the phase velocity is near the rotation velocity. The turbulence with small wavenumber in the bad-curvature region disappears in OH plasmas. In addition, the small component which propagates in the ion diamagnetic drift direction is also observed in NBI plasmas.

ACKNOWLEDGMENT

References

1) J. C. Jobes, and R. L. Hickok, Nuclear Fusion **10**(1970) 195.

2) G. A. Hallock, J. Mathew, W. C . Jennings, R. L. Hickok, K. A. Conner, A. J. Wooton,and R. C. Isler, Phys. Rev. Lett **56** (1986) 1248.

3) T. P. Crowley et al., Nuclear Fusion **32** (1992) 1295.

4) D. W. Ross et al., Nuclear Fusion **31** (1991) 1355.

5) J. W. Heard et al., Phys. Plasmas **2**, 3360 (1995).

6) Y. Hamada et al., in *Proceedings of the 15h International Conference on Plasma Physics and Controlled Nuclear Fusion Research, Seville, 1994* (IAEA, Vienna), Vol.1, p.301 (1993).

7) M. Okabayashi and V. Arunsalam, Nuclear Fusion **17** (1977) 497.

8) T. Crowley and E. Mazzucato, Nuclear Fusion **25** (1985) 507.

9) D. L. Brower, W. A. Peebles, N. C. Luhmann, Jr., Nuclear Fusion **27** (1987) 2055.

10) R. J. Fonck et al., Phys. Rev. Lett., **70** (1993) 3736.

11) R. D. Durst et al., Phys. Rev. Lett., **71** (1993) 3135.

12) K. Toi et al., in *Proceedings of the 14h International Conference on Plasma Physics and Controlled Nuclear Fusion Research, Wurzburg, 1992* (IAEA, Vienna), Vol.1, p.301 (1993).

13) Y. Hamada et al., Plasma Phys. Control. Fusion **36** (1994) 1743.

14) Y. Hamada et al., Rev. Sci. Instrum. **66** (1995) 321.

15) Y. Hamada et al., Nuclear Fusion **36** (1996) 515.

16) T. S. Green and G. A. Proca, Rev. Sci. Instrum. **41** (1970) 1409.

17) Y. Hamada et al., Rev. Sci. Instrum. **63** (1992) 4446.

[18] L. Solensten and K. A. Connor, Rev. Sci. Instrum. **58** (1987) 516.

19) K. Narihara et al., Japan. J. appl. Phys. **35** (1996) 266.

20) X. Z. Yang et al., Phys. Fluids. B **3** (1991) 3448.

21) K. Ida et al., Rev. Sci. Instrum. **57** (1986) 1825.

22) Ch. P. Ritz et al., Phys. Fluids. **27** (1984) 2956.

23) Ch. P. Ritz et al., Phys. Rev. Lett., **65** (1990) 2543.

24) M. Endler et al., Nuclear Fusion **35** (1995) 1307.

25) K. Ida et al., Nuclear Fusion **31** (1991) 943.

26) D. W. Ross et al., Rev. Sci. Instrum. **63** (1992) 2232.

Figure captions

Figure 1(a). The setup of a heavy ion beam probe for JIPP T-IIU. The lower electrode in

the analyzer is the vessel itself. 1(b). Typical behaviour of the total and kinetic energy of

the primary and secondary beam to illustrate the basic principle of the potential

measurement in the plasma by a heavy ion beam probe. By the increase of the charge

number from 1 to 2 in ionization, the total and potential energy of the secondary beam

increases by $e\Phi(r_x)$, where r_x is the place where the ionization takes place. Because of

total energy conservation, the kinetic energy of the secondary beam outside the plasma

deviates from the initial energy at the injection by $e\Phi(r_x)$. This change of the energy is

measured by an energy analyzer.

Figure 2. Calculated data of position and the shape of 7 sample volumes of the heavy ion

beam probe in JIPP T-IIU when the primary beam (450, 350, 300, 250, 200 keV) is

swept in steps by the sweeper at the entrance to the tokamak as shown in Fig. 1 at 3 Tesla

operation. The sweep angle at the poloidal sweeper at step m at 450 keV is θ_m=0.4m-

0.9, and a set of sweep angle of [-0.5, -0.1, 0.3, 0.7, 1.1, 1.5, 1.8] is adopted in this

figure. The expanded view of sample volumes at steps 6 and 7 for at 450 keV beam is

also shown in Fig, 2(b). The beam is assumed to be a parallel beam of the diameter of 1.5

mm.

Figure 3. Raw data of the intensity of the secondary beam currents (sums of currents to the

upper and lower detector plates) from 6 sample volumes, when sample volumes are swept

in steps as shown in Fig. 2. Thallium beam energy is 450 keV and the toroidal field is 3

Tesla. NBI heated plasma.

Figure 4. Electron temperature (a) and electron density (b) profiles measured by YAG

laser Thomson scattering method with the repetition rate of 100 Hz. Profiles at every 20

ms are shown. Those are shifted upwards by 2 keV for (a) and $3 \times 10^{13} cm^{-3}$ for (b) to avoid confusion. The first profile shown here is at 160 ms from the start of the plasma discharge. The NBI started at 175 ms. Also shown are electron diamagnetic drift velocity calculated from the data of (a) and (b).

Figure 5. The evolution of the radial potential profile (dashed curve) from startup to NBI heated plasma in JIPP T-IIU tokamak. The radial profiles were obtained every 2.5 ms by 400 Hz radial sweep and fast 5 kHz toroidal sweep of the primary beam. The profiles at every 20 ms are shown in this figure. The first profile is about 3 ms after the application of the toroidal electric field and at the breakdown phase of the toroidal discharge. NBI starts in this case at 100 ms in this case.

Figure 6. Changes of the ion temperature profiles in NBI heated plasmas measured by a charge recombination spectroscopy.
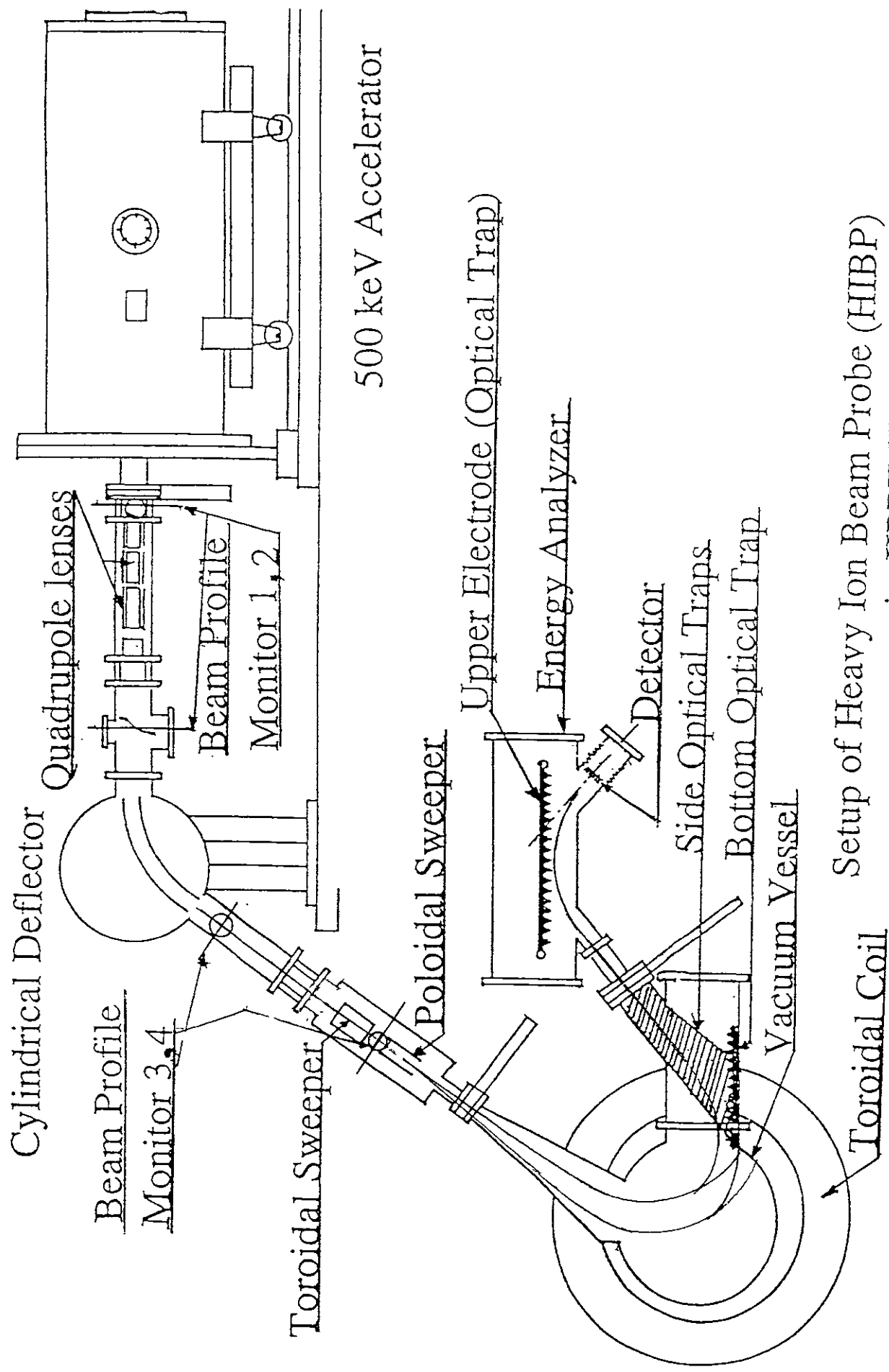
Figure 7. 6 correlation coefficient functions $\rho_{1,j}(t)$, j=1, 2, 3, 4, 5, 6 of the intensity (sum) of the secondary currents from the sample volume 1 with the intensities from 6 sample volumes (s_j, j =1 to 6) at each steps (1 to 6) of Fig. 2. Also contours of wavenumber/frequency spectrum density $S(k,\omega)$ of these 6 normalized intensity, $\dfrac{\tilde{s_j}}{s_j}$, are also shown. The thallium beam energy is 450 for (a), 350 keV for (b) , 300 keV for (c) , 250 keV for (d) and 200 keV for (e). The positive wavenumber in $S(k,\omega)$ and the shift of the peak of the correlation curve to negative delay time, correspond to the electron diamagnetic drift direction. The j-th line in the contour corresponds to the intensity of $\max(S(k,\omega))$ x e^{-j}. The toroidal field is 3 Tesla. The number of the slits of the energy analyzer is 7 (7 sample volumes) and 1 to 6 sample volume are measured. $\rho_{1,j}(t)$ is shifted upwards by j to avoid confusion. In case of (c) and (d), there is no signals at sample volume 2 in order to check the total noise level.

Figure 8. 6 correlation coefficient functions $\rho_{1,j}(t)$, j=1, 2 , 3, 4, 5, 6 and contours of wavenumber/frequency spectrum density $S(k,\omega)$ of the intensity (sum) of the secondary currents for OH plasmas. The beam energy is 350 keV for (a) and 300 keV for (b).

Figure 9. Correlation coefficient functions and contours under detailed scan around step 2 and 3 of Fig. 7 (a). The sweep angle is $\theta_m=0.16m - 0.4$, [-0.24, -0.08, 0.08, 0.24], compared to $\theta_m=0.4m-0.9$ in case of Fig. 7 (a). The frequency range is expanded to -300 kHz to 300 kHz.
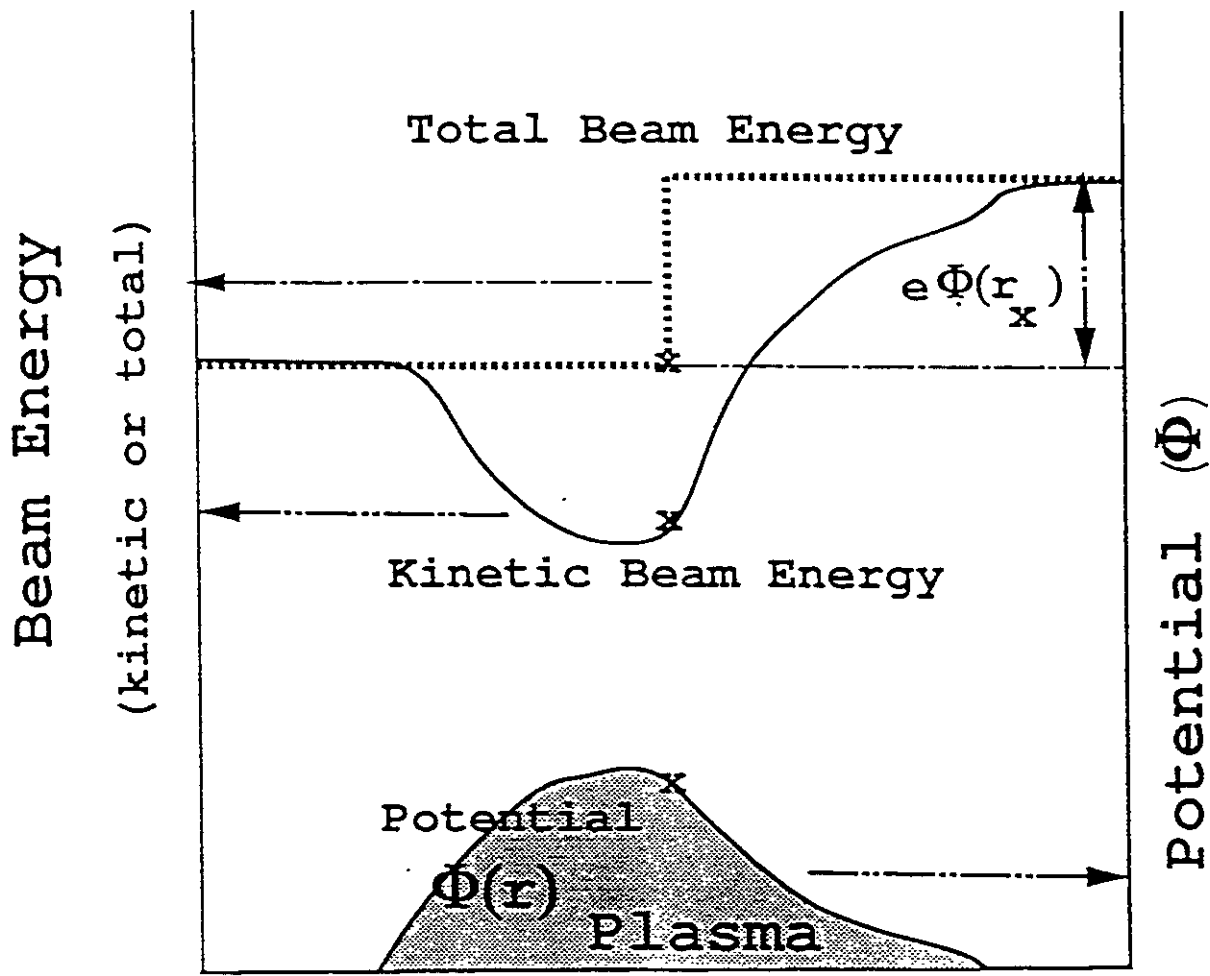
Figure 10. Comparison of $S(k,\omega)$ without compensation, (a) and with the compensation of the path integral effect, (b) . 350 keV. In Fig. 10 (b), 5 signals $\dfrac{\tilde{s_j}}{s_j}-\dfrac{\tilde{s_6}}{s_6}$, i=1, 2, 3, 4, 5 are 2 dimensionally Fourier analyzed, while Fig. 10(a) is based on $\dfrac{\tilde{s_j}}{s_j}$, j=1 to 6, for comparison. Fig. 10(a) is identical with the contours of $S(k,\omega)$ in Fig. 7(b).

Table 1. Calculated position and length of sample volumes of Fig. 3. The beam radius of 1.5 mm is assumed at the poloidal sweeper at the entrance to the tokamak. Eb is the beam energy in keV. r(cm), t1 is the minor radius and angle of the center of SV 3 (the third sample volume as shown in Fig. 3(b)) at each step. It is assumed the axis is at 93 cm. dl is the distance between the centers of SV 3 and SV 4. dll is the length of the longer diagonal of SV 3. t2 is the angle of direction of the longer diagonal.

Cylindrical Deflector

Quadrupole lenses

500 keV Accelerator

Beam Profile Monitor 1, 2

Beam Profile Monitor 3, 4

Toroidal Sweeper

Poloidal Sweeper

Upper Electrode (Optical Trap)

Energy Analyzer

Detector

Side Optical Traps

Bottom Optical Trap

Vacuum Vessel

Toroidal Coil

Setup of Heavy Ion Beam Probe (HIBP) in JIPPT-IIU

Fig. 1 (a)

Fig. 1 (b)

Fig. 2

(a)

Major radius (mm)

450 keV Plasma boundary 250 keV 200 keV 300 keV

350 keV

Step1 Step2 Step3 Step4 Step5 Step6 Step7

200.0 100.0 0.0 -100.0

900.0 1000.0 1100.0 1200.0

(b)

Major radius (mm)

Step 5 Step 6 Step 7

SV 7 SV 6 SV 5 SV 4 SV 3 SV 2 SV 1

40.0 20.0 0.0 -20.0 -40.0
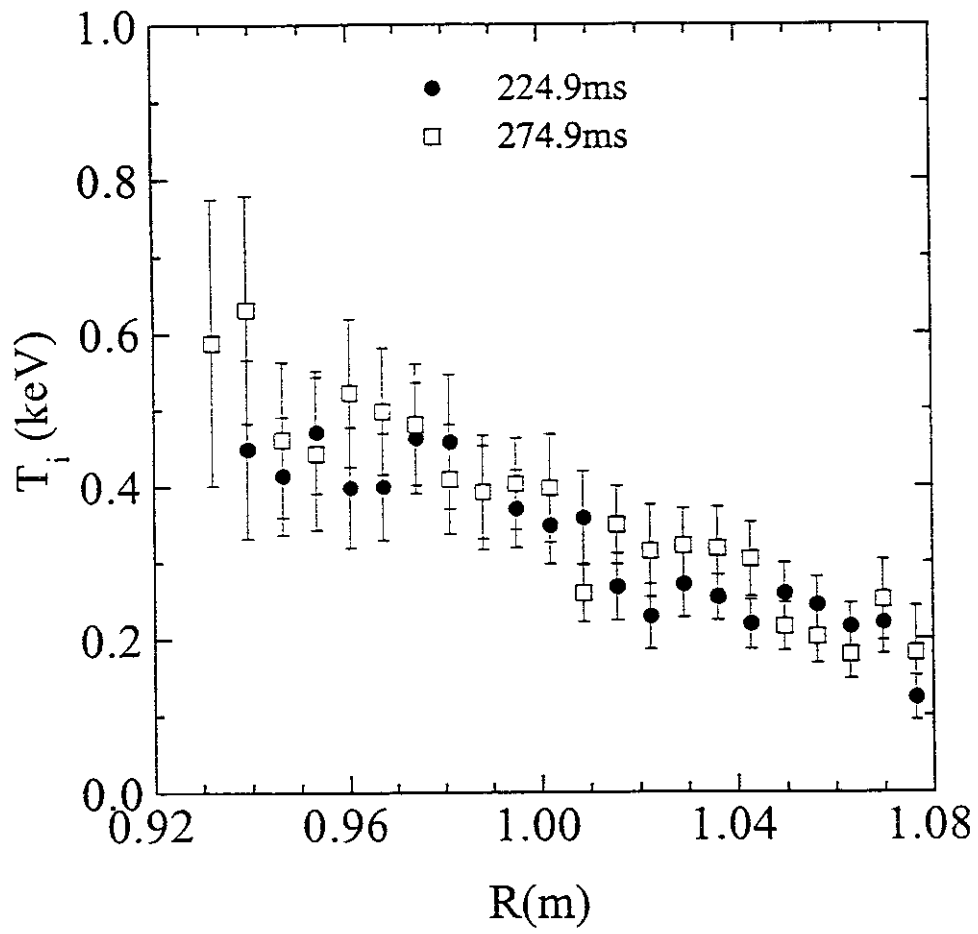
950.0 1000.0
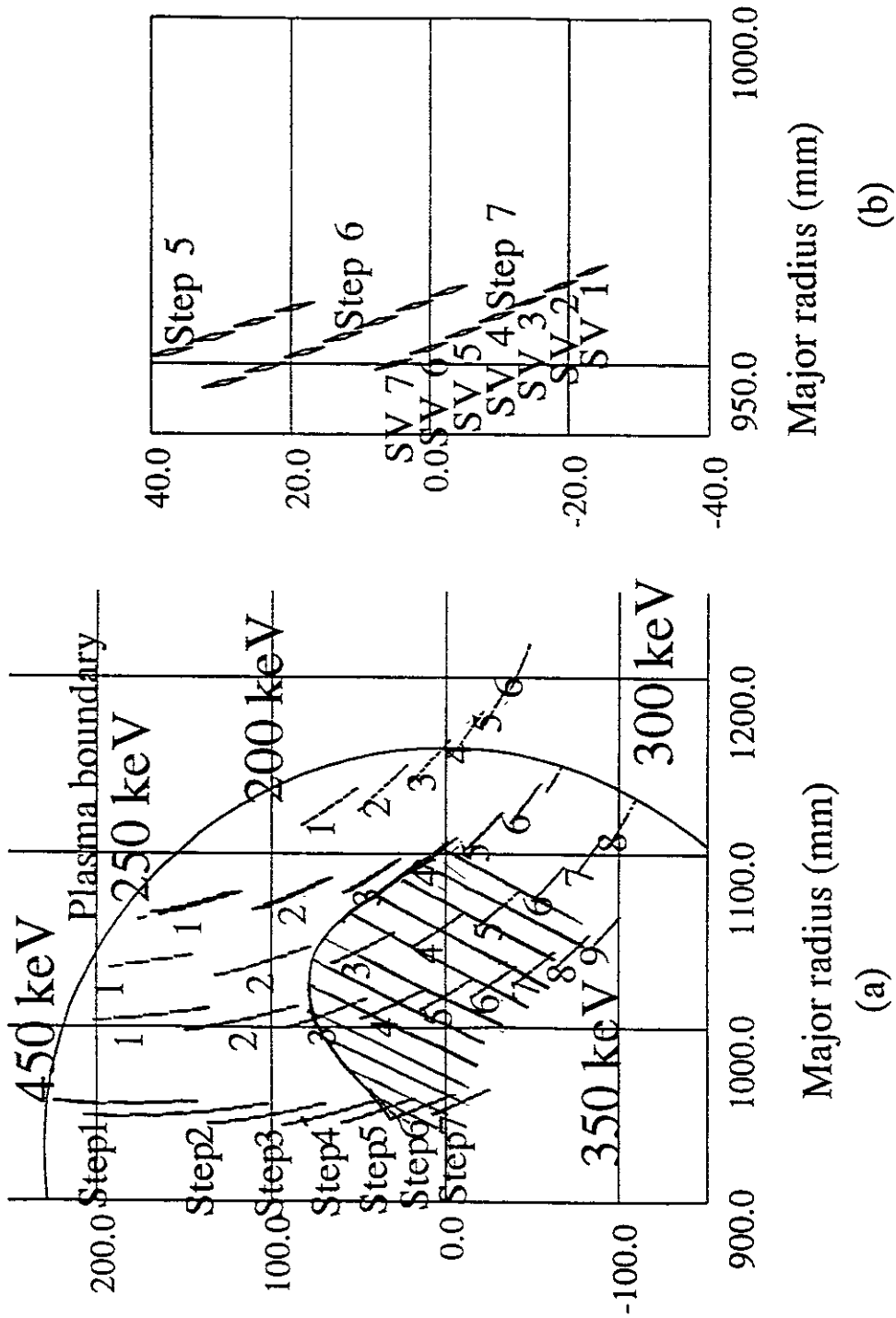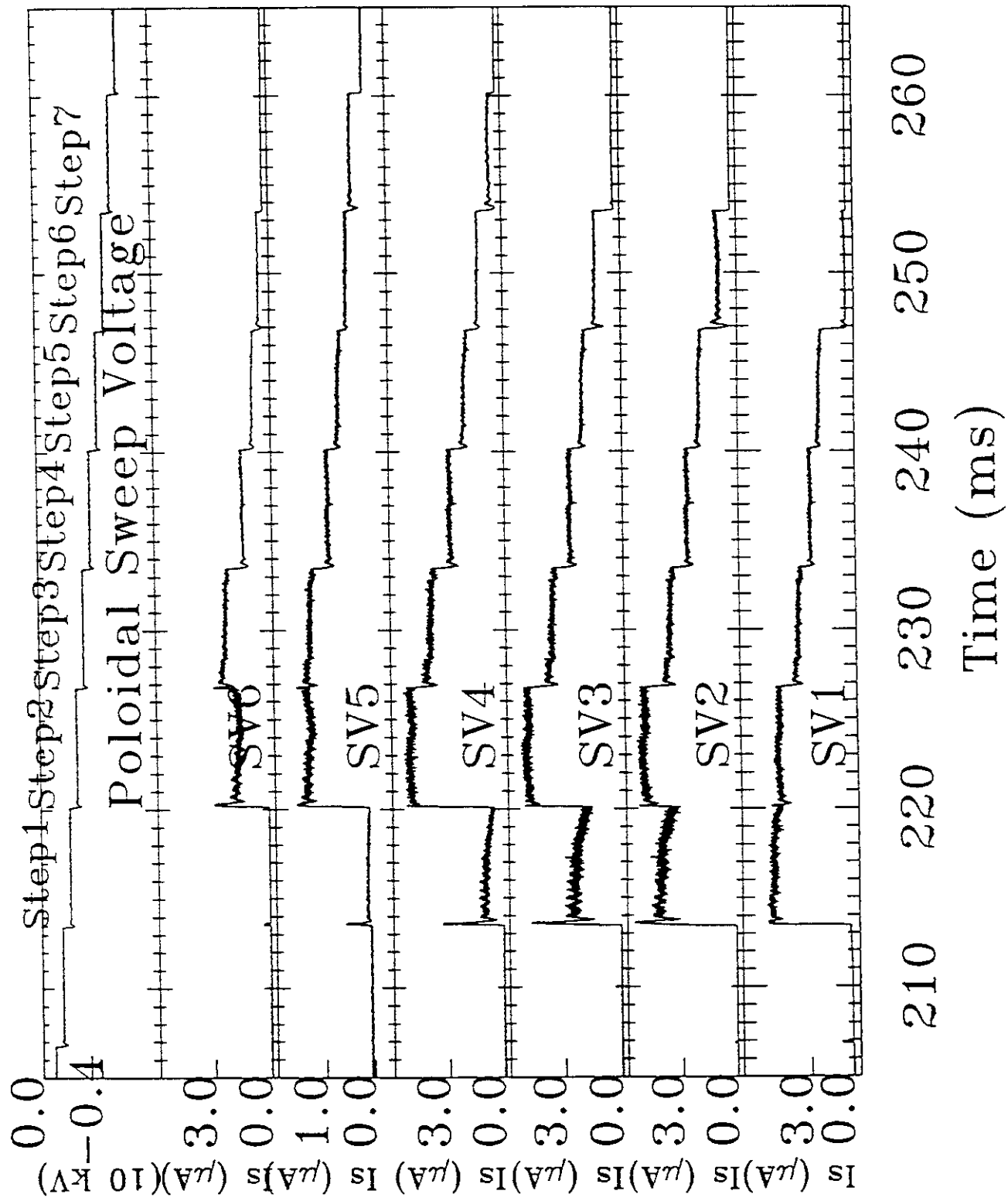
Fig. 3
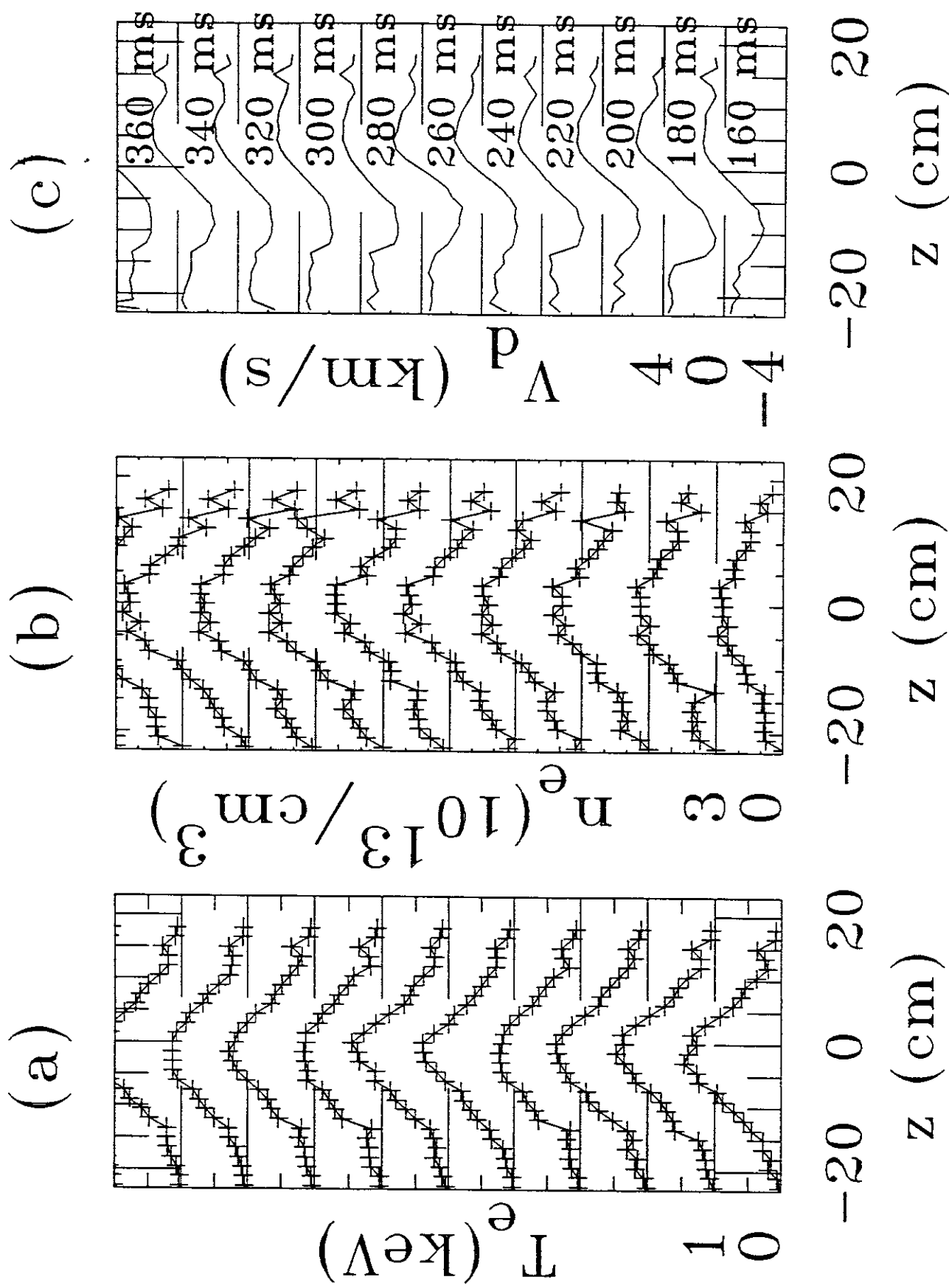
Fig. 4
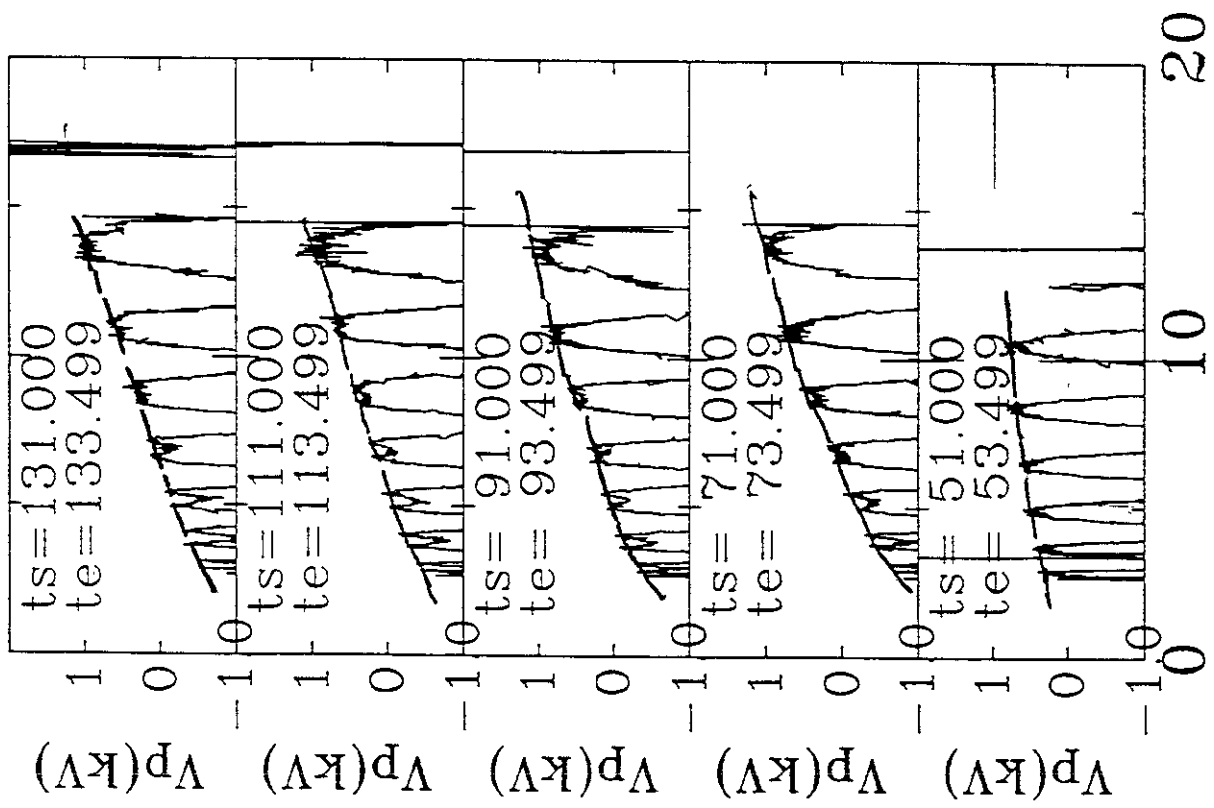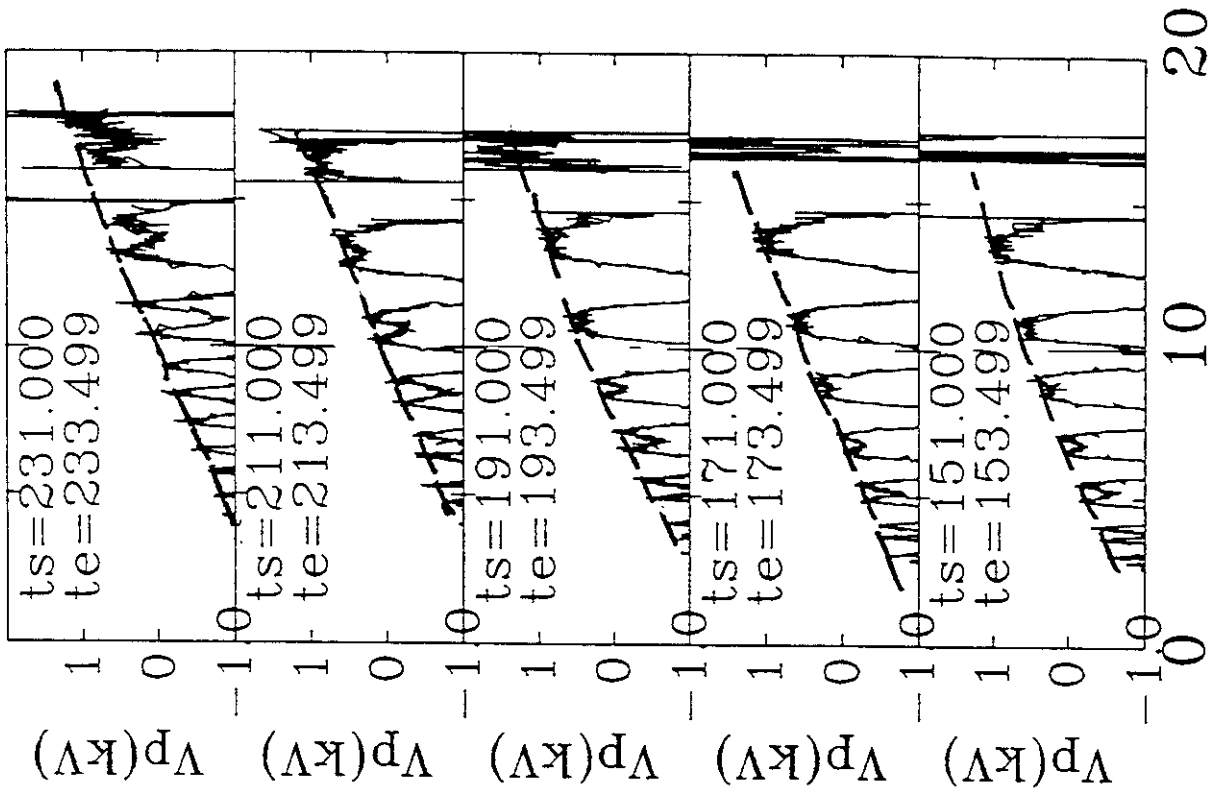
Fig. 5

Fig. 6
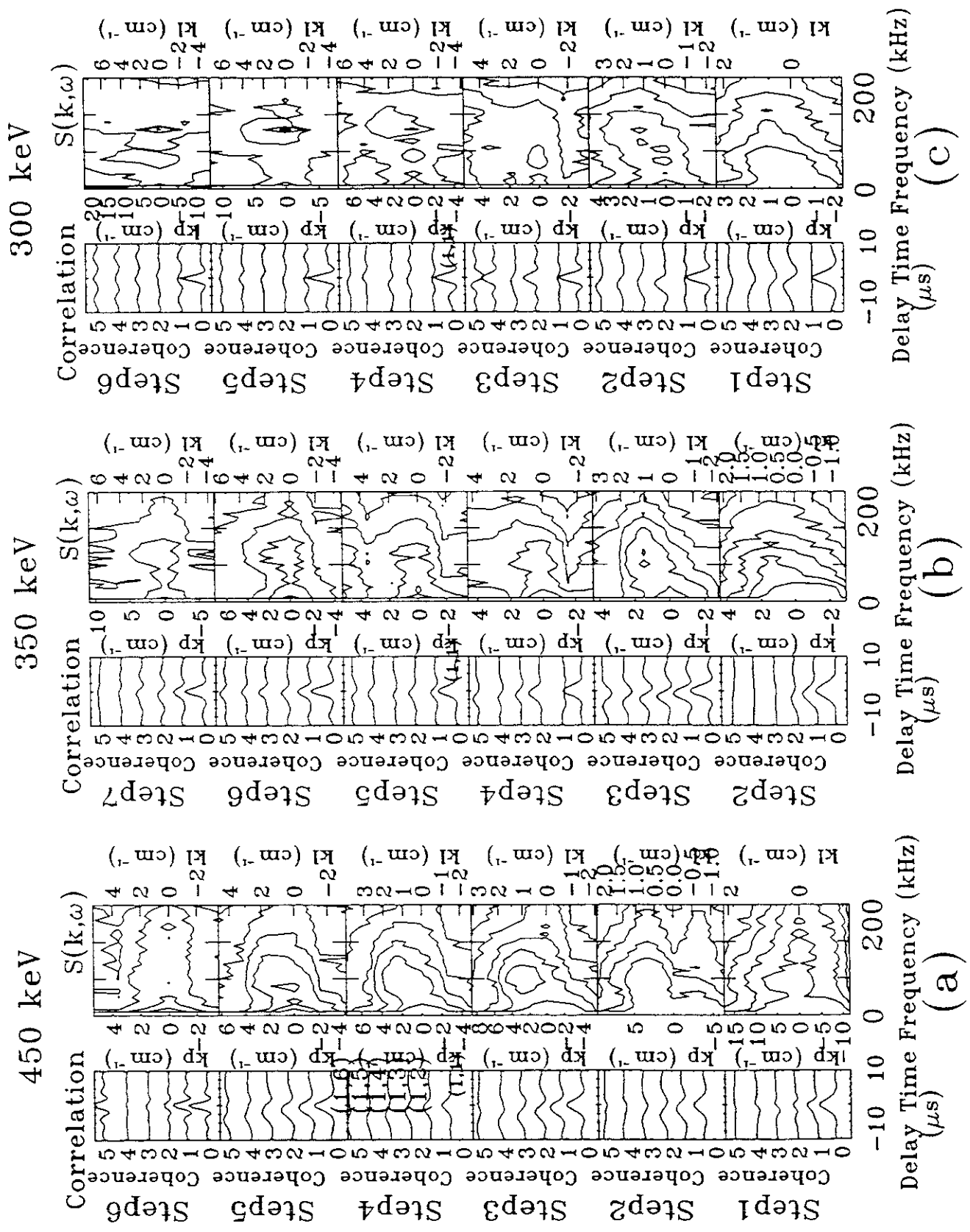
Fig. 7

Fig. 7
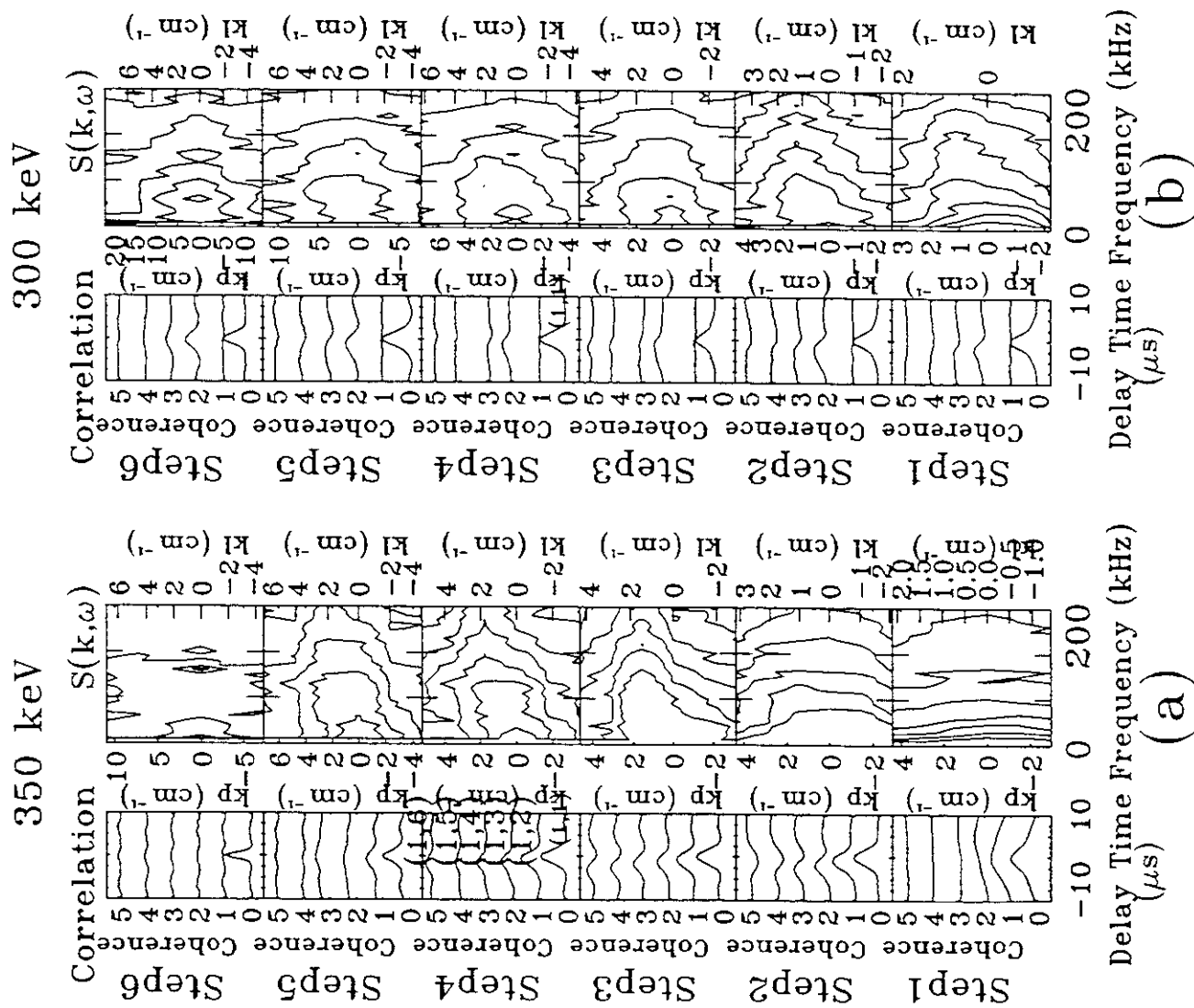
Fig. 8
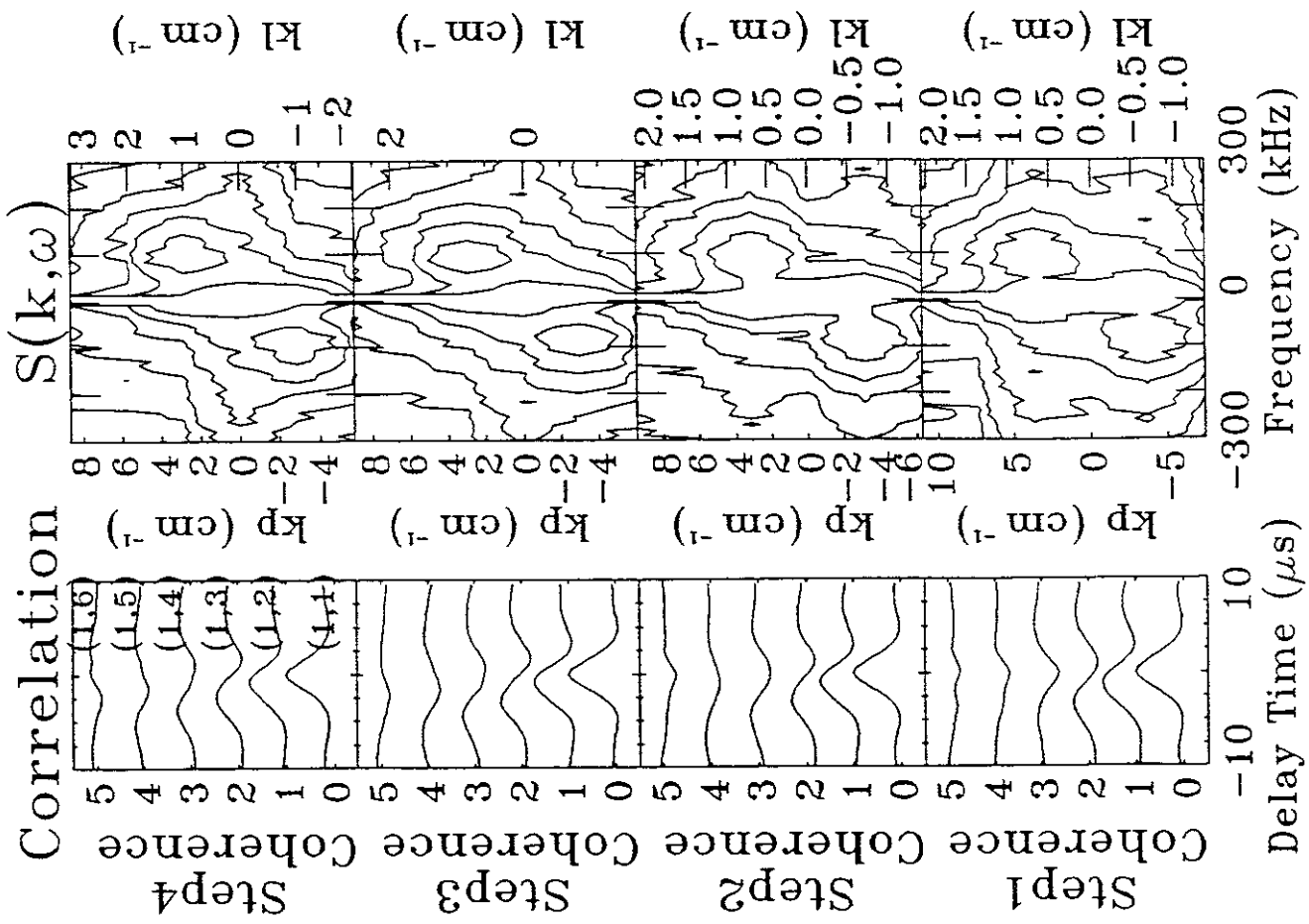
Fig. 9
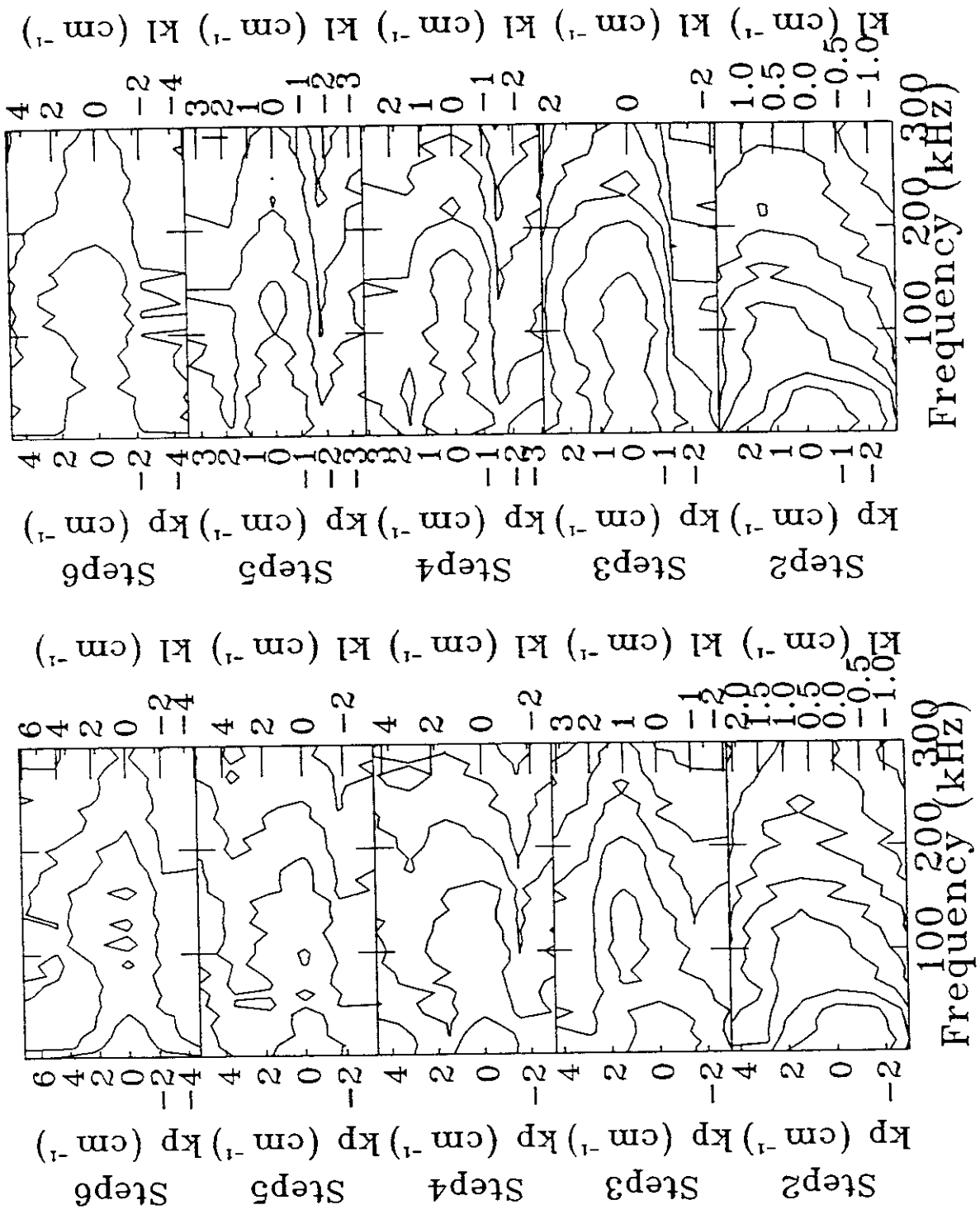
Fig. 10

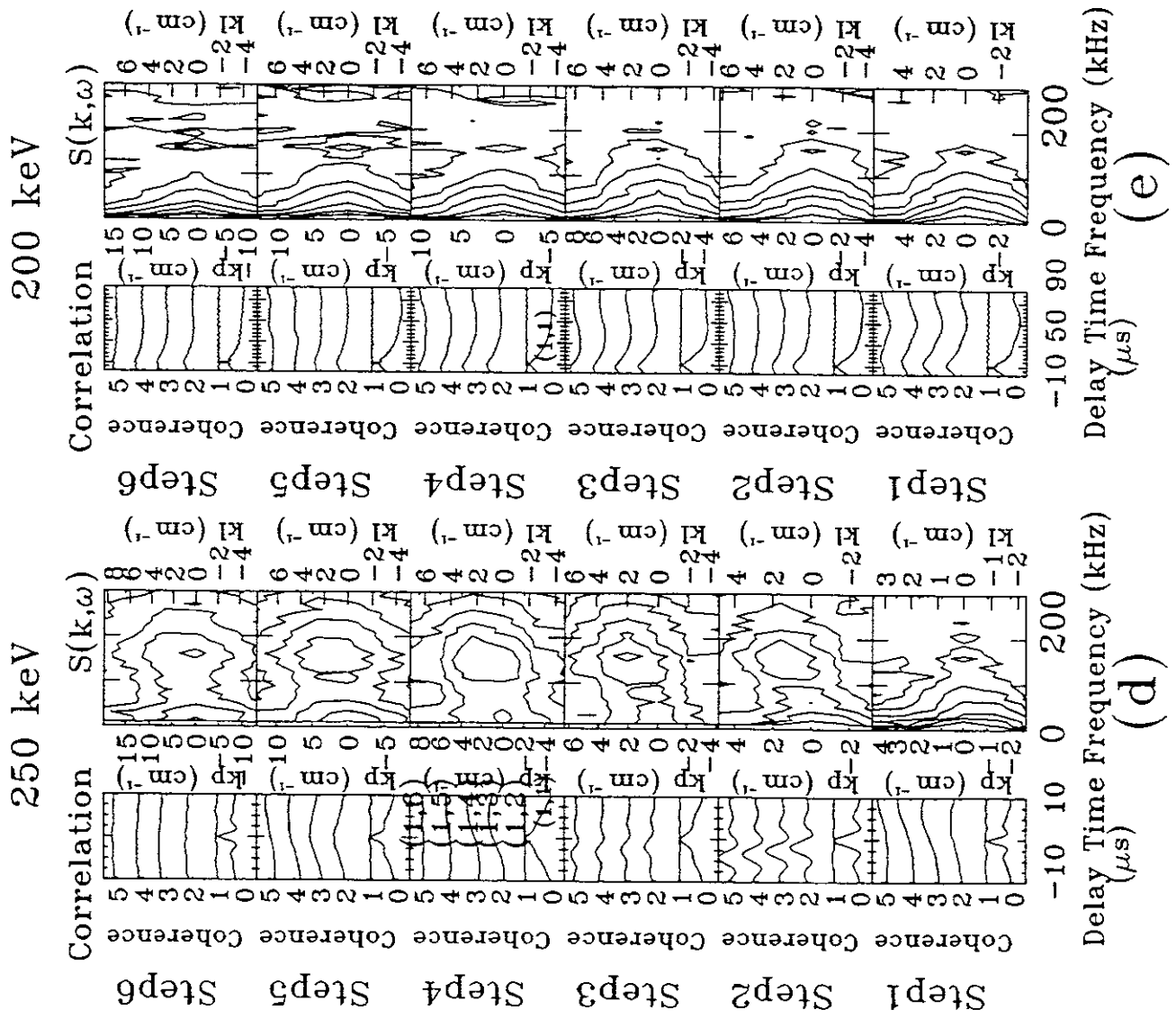| Eb	Step	r(cm)	t1(deg.)	d1(cm)	d11(cm)	t2(deg.)
200	1	20.76	18.65	0.56	0.47	−60.74
200	2	20.98	11.74	0.50	0.42	−55.03
200	3	21.61	5.96	0.46	0.38	−48.96
200	4	22.52	1.28	0.44	0.36	−43.71
200	5	23.64	−2.42	0.42	0.34	−37.83
200	6	24.91	−5.25	0.41	0.33	−32.71
250	1	20.44	46.99	0.94	1.82	−82.52
250	2	17.05	30.39	0.63	1.13	−74.18
250	3	16.26	14.77	0.50	0.88	−66.38
250	4	16.94	2.08	0.44	0.74	−58.28
250	5	18.46	−7.07	0.40	0.66	−49.53
250	6	20.44	−13.14	0.38	0.61	−40.17
300	1	42.33	−12.90	52.58	105.17	10.13
300	2	14.87	43.45	0.80	0.73	−76.82
300	3	12.47	21.89	0.59	0.54	−69.18
300	4	12.60	1.73	0.50	0.44	−61.70
300	5	14.19	−12.59	0.44	0.39	−54.24
300	6	16.44	−21.32	0.40	0.35	−46.10
350	1	19.69	67.59	1.60	1.64	−88.59
350	2	13.57	56.48	0.92	0.89	−81.40
350	3	10.28	40.51	0.70	0.65	−75.54
350	4	8.83	19.76	0.58	0.53	−70.28
350	5	8.92	−0.84	0.50	0.47	−65.36
350	6	10.06	−16.38	0.45	0.42	−60.86
450	1	21.00	82.91	2.55	3.03	85.67
450	2	14.19	81.66	1.26	1.32	−88.40
450	3	10.03	78.76	0.93	0.94	−84.19
450	4	6.83	72.89	0.75	0.76	−80.81
450	5	4.31	59.88	0.65	0.66	−77.75
450	6	2.70	27.75	0.57	0.58	−74.70

Table 1.

Recent Issues of NIFS Series

NIFS-423   Joong-San Koog,
Development of an Imaging VUV Monochromator in Normal Incidence Region. July 1996

NIFS-424   K. Orito,
A New Technique Based on the Transformation of Variables for Nonlinear Drift and Rossby Vortices; July 1996

NIFS-425   A. Fujisawa, H. Iguchi, S. Lee, T.P. Crowley, Y. Hamada, H. Sanuki, K. Itoh, S. Kubo, H. Idei, T. Minami, K. Tanaka, K. Ida, S. Nishimura, S. Hidekuma, M. Kojima, C. Takahashi, S. Okamura and K. Matsuoka,
Direct Observation of Potential Profiles with a 200keV Heavy Ion Beam Probe and Evaluation of Loss Cone Structure in Toroidal Helical Plasmas on the Compact Helical System; July 1996

NIFS-426   H. Kitauchi, K. Araki and S. Kida,
Flow Structure of Thermal Convection in a Rotating Spherical Shell; July 1996

NIFS-427   S. Kida and S. Goto,
Lagrangian Direct-interaction Approximation for Homogeneous Isotropic Turbulence; July 1996

NIFS-428   V.Yu. Sergeev, K.V. Khlopenkov, B.V. Kuteev, S. Sudo, K. Kondo, F. Sano, H. Zushi, H. Okada, S. Besshou, T. Mizuuchi, K. Nagasaki, Y. Kurimoto and T. Obiki,
Recent Experiments on Li Pellet Injection into Heliotron E; Aug. 1996

NIFS-429   N. Noda, V. Philipps and R. Neu,
A Review of Recent Experiments on W and High Z Materials as Plasma-Facing Components in Magnetic Fusion Devices; Aug. 1996

NIFS-430   R.L. Tobler, A. Nishimura and J. Yamamoto,
Design-Relevant Mechanical Properties of 316-Type Stainless Steels for Superconducting Magnets; Aug. 1996

NIFS-431   K. Tsuzuki, M. Natsir, N. Inoue, A. Sagara, N. Noda, O. Motojima, T. Mochizuki, T. Hino and T. Yamashina,
Hydrogen Absorption Behavior into Boron Films by Glow Discharges in Hydrogen and Helium; Aug. 1996

NIFS-432   T.-H. Watanabe, T. Sato and T. Hayashi,
Magnetohydrodynamic Simulation on Co- and Counter-helicity Merging of Spheromaks and Driven Magnetic Reconnection; Aug. 1996

NIFS-433   R. Horiuchi and T. Sato,

Particle Simulation Study of Collisionless Driven Reconnection in a Sheared Magnetic Field; Aug. 1996

NIFS-434   Y. Suzuki, K. Kusano and K. Nishikawa,
Three-Dimensional Simulation Study of the Magnetohydrodynamic Relaxation Process in the Solar Corona. II.; Aug. 1996

NIFS-435   H. Sugama and W. Horton,
Transport Processes and Entropy Production in Toroidally Rotating Plasmas with Electrostatic Turbulence; Aug. 1996

NIFS-436   T. Kato, E. Rachlew-Källne, P. Hörling and K.-D Zastrow,
Observations and Modelling of Line Intensity Ratios of OV Multiplet Lines for 2s3s 3S1 - 2s3p 3Pj; Aug. 1996

NIFS-437   T. Morisaki, A. Komori, R. Akiyama, H. Idei, H. Iguchi, N. Inoue, Y. Kawai, S. Kubo, S. Masuzaki, K. Matsuoka, T. Minami, S. Morita, N. Noda, N. Ohyabu, S. Okamura, M. Osakabe, H. Suzuki, K. Tanaka, C. Takahashi, H. Yamada, I. Yamada and O. Motojima,
Experimental Study of Edge Plasma Structure in Various Discharges on Compact Helical System; Aug. 1996

NIFS-438   A. Komori, N. Ohyabu, S. Masuzaki, T. Morisaki, H. Suzuki, C. Takahashi, S. Sakakibara, K. Watanabe, T. Watanabe, T. Minami, S. Morita, K. Tanaka, S. Ohdachi, S. Kubo, N. Inoue, H. Yamada, K. Nishimura, S. Okamura, K. Matsuoka, O. Motojima, M. Fujiwara, A. Iiyoshi, C. C. Klepper, J.F. Lyon, A.C. England, D.E. Greenwood, D.K. Lee, D.R. Overbey, J.A. Rome, D.E. Schechter and C.T. Wilson,
Edge Plasma Control by a Local Island Divertor in the Compact Helical System; Sep. 1996 (IAEA-CN-64/C1-2)

NIFS-439   K. Ida, K. Kondo, K. Nagaski T. Hamada, H. Zushi, S. Hidekuma, F. Sano, T. Mizuuchi, H. Okada, S. Besshou, H. Funaba, Y. Kurimoto, K. Watanabe and T. Obiki,
Dynamics of Ion Temperature in Heliotron-E; Sep. 1996 (IAEA-CN-64/CP-5)

NIFS-440   S. Morita, H. Idei, H. Iguchi, S. Kubo, K. Matsuoka, T. Minami, S. Okamura, T. Ozaki, K. Tanaka, K. Toi, R. Akiyama, A. Ejiri, A. Fujisawa, M. Fujiwara, M. Goto, K. Ida, N. Inoue, A. Komori, R. Kumazawa, S. Masuzaki, T. Morisaki, S. Muto, K. Narihara, K. Nishimura, I. Nomura, S. Ohdachi, M.. Osakabe, A. Sagara, Y. Shirai, H. Suzuki, C. Takahashi, K. Tsumori, T. Watari, H. Yamada and I. Yamada,
A Study on Density Profile and Density Limit of NBI Plasmas in CHS; Sep. 1996 (IAEA-CN-64/CP-3)

NIFS-441   O. Kaneko, Y. Takeiri, K. Tsumori, Y. Oka, M. Osakabe, R. Akiyama, T. Kawamoto, E. Asano and T. Kuroda,
Development of Negative-Ion-Based Neutral Beam Injector for the Large

Helical Device; Sep. 1996 (IAEA-CN-64/GP-9)

NIFS-442 K. Toi, K.N. Sato, Y. Hamada, S. Ohdachi, H. Sakakita, A. Nishizawa, A. Ejiri, K. Narihara, H. Kuramoto, Y. Kawasumi, S. Kubo, T. Seki, K. Kitachi, J. Xu, K. Ida, K. Kawahata, I. Nomura, K. Adachi, R. Akiyama, A. Fujisawa, J. Fujita, N. Hiraki, S. Hidekuma, S. Hirokura, H. Idei, T. Ido, H. Iguchi, K. Iwasaki, M. Isobe, O. Kaneko, Y. Kano, M. Kojima, J. Koog, R. Kumazawa, T. Kuroda, J. Li, R. Liang, T. Minami, S. Morita, K. Ohkubo, Y. Oka, S. Okajima, M. Osakabe, Y. Sakawa, M. Sasao, K. Sato, T. Shimpo, T. Shoji, H. Sugai, T. Watari, I. Yamada and K. Yamauti,
Studies of Perturbative Plasma Transport, Ice Pellet Ablation and Sawtooth Phenomena in the JIPP T-IIU Tokamak; Sep. 1996 (IAEA-CN-64/A6-5)

NIFS-443 Y. Todo, T. Sato and The Complexity Simulation Group,
Vlasov-MHD and Particle-MHD Simulations of the Toroidal Alfvén Eigenmode; Sep. 1996 (IAEA-CN-64/D2-3)

NIFS-444 A. Fujisawa, S. Kubo, H. Iguchi, H. Idei, T. Minami, H. Sanuki, K. Itoh, S. Okamura, K. Matsuoka, K. Tanaka, S. Lee, M. Kojima, T.P. Crowley, Y. Hamada, M. Iwase, H. Nagasaki, H. Suzuki, N. Inoue, R. Akiyama, M. Osakabe, S. Morita, C. Takahashi, S. Muto, A. Ejiri, K. Ida, S. Nishimura. K. Narihara, I. Yamada, K. Toi, S. Ohdachi, T. Ozaki, A. Komori, K. Nishimura, S. Hidekuma, K. Ohkubo, D.A. Rasmussen, J.B. Wilgen, M. Murakami, T. Watari and M. Fujiwara,
An Experimental Study of Plasma Confinement and Heating Efficiency through the Potential Profile Measurements with a Heavy Ion Beam Probe in the Compact Helical System; Sep. 1996 (IAEA-CN-64/C1-5)

NIFS-445 O. Motojima, N. Yanagi, S. Imagawa, K. Takahata. S. Yamada, A. Iwamoto, H. Chikaraishi, S. Kitagawa, R. Maekawa, S. Masuzaki, T. Mito, T. Morisaki, A. Nishimura, S. Sakakibara, S. Satoh, T. Satow, H. Tamura, S. Tanahashi, K. Watanabe, S. Yamaguchi, J. Yamamoto, M.Fujiwara and A. Iiyoshi,
Superconducting Magnet Design and Construction of LHD; Sep. 1996 (IAEA-CN-64/G2-4)

NIFS-446 S. Murakami, N. Nakajima, S. Okamura, M. Okamoto and U. Gasparino,
Orbit Effects of Energetic Particles on the Reachable β-Value and the Radial Electric Field in NBI and ECR Heated Heliotron Plasmas; Sep. 1996 (IAEA-CN-64/CP -6) Sep. 1996

NIFS-447 K. Yamazaki, A. Sagara, O. Motojima, M. Fujiwara, T. Amano, H. Chikaraishi, S. Imagawa, T. Muroga, N. Noda, N. Ohyabu, T. Satow, J.F. Wang, K.Y. Watanabe, J. Yamamoto . H. Yamanishi, A. Kohyama, H. Matsui, O. Mitarai, T. Noda, A.A. Shishkin, S. Tanaka and T. Terai
Design Assessment of Heliotron Reactor; Sep. 1996 (IAEA-CN-64/G1-5)

NIFS-448 M. Ozaki, T. Sato and the Complexity Simulation Group.
Interactions of Convecting Magnetic Loops and Arcades; Sep. 1996

NIFS-449 T. Aoki,

Differential Equations; Sep. 1996

NIFS-450   D. Biskamp and T. Sato,
            Partial Reconnection in the Sawtooth Collapse; Sep. 1996

NIFS-451   J. Li, X. Gong, L. Luo, F.X. Yin, N. Noda, B. Wan, W. Xu, X. Gao, F. Yin, J.G.
            Jiang, Z. Wu., J.Y. Zhao, M. Wu, S. Liu and Y. Han,
            Effects of High Z Probe on Plasma Behavior in HT-6M Tokamak; Sep. 1996

NIFS-452   N. Nakajima, K. Ichiguchi, M. Okamoto and R.L. Dewar,
            Ballooning Modes in Heliotrons/Torsatrons; Sep. 1996 (IAEA-CN-64/D3-6)

NIFS-453   A. Iiyoshi,
            Overview of Helical Systems; Sep. 1996 (IAEA-CN-64/O1-7)

NIFS-454   S. Saito, Y. Nomura, K. Hirose and Y.H. Ichikawa,
            *Separatrix Reconnection and Periodic Orbit Annihilation in the Harper
            Map*; Oct. 1996

NIFS-455   K. Ichiguchi, N. Nakajima and M. Okamoto,
            Topics on MHD Equilibrium and Stability in Heliotron / Torsatron; Oct.
            1996

NIFS-456   G. Kawahara, S. Kida, M. Tanaka and S. Yanase,
            *Wrap, Tilt and Stretch of Vorticity Lines around a Strong Straight Vortex Tube
            in a Simple Shear Flow*; Oct. 1996

NIFS-457   K. Itoh, S.- I. Itoh, A. Fukuyama and M. Yagi,
            Turbulent Transport and Structural Transition in Confined Plasmas; Oct.
            1996

NIFS-458   A. Kageyama and T. Sato,
            *Generation Mechanism of a Dipole Field by a Magnetohydrodynamic
            Dynamo*; Oct. 1996

NIFS-459   K. Araki, J. Mizushima and S. Yanase,
            The Non-axisymmetric Instability of the Wide-Gap Spherical Couette Flow;
            Oct. 1996

NIFS-460   Y. Hamada, A. Fujisawa, H. Iguchi, A. Nishizawa and Y. Kawasumi,
            A Tandem Parallel Plate Analyzer; Nov. 1996

NIFS-461   Y. Hamada, A. Nishizawa, Y. Kawasumi, A. Fujisawa, K. Narihara, K. Ida, A. Ejiri,
            S. Ohdachi, K. Kawahata, K. Toi, K. Sato, T. Seki, H. Iguchi, K. Adachi, S. Hidekuma,
            S.Hirokura, K. Iwasaki, T. Ido, M. Kojima, J. Koong, R. Kumazawa, H. Kuramoto,
            T. Minami, I. Nomura, H. Sakakita, M. Sasao, K.N. Sato, T. Tsuzuki, J. Xu, I. Yamada and
            T. Watari,
            *Density Fluctuation in JIPP T-IIU Tokamak Plasmas Measured by a Heavy
            Ion Beam Probe*; Nov. 1996